Technical University of Munich
Department of Physics
Dense and Strange Hadronic Matter group

Femtoscopy studies of nucleon-hyperon potentials and Ξ^- production in 13 TeV pp collisions at ALICE

Bachelorarbeit

Themensteller:	Prof. Dr. Laura Fabbietti
Betreuer:	Dimitar L. Mihaylov, M.Sc.
Ausgabe:	July 01, 2018
Abgabe:	October 08, 2018

Table of Contents

1 Introduction

Neutron stars are amongst the most fascinating objects in the cosmos. They are formed during supernovae, when the inner core of a heavy star of several solar masses collapses under its gravitational pressure. Due to the collapse, the density increases rapidly, up to the point when it becomes energetically more favorable to convert protons and electrons to neutrons and neutrinos through the inverse beta decay. The remaining mass of the collapse is a neutron star with a mass of maximum two solar masses compressed in a radius of 10 to 13 km, making this star even denser than nuclear matter ($\rho_0 \approx 0.17\, fm^{-3}$). Other extreme properties like strong magnetic fields or spin periods in the range of milliseconds exist as well, which make neutron stars highly interesting research targets.

The most interesting open question is what the inner layers and the core are made of. There are multiple theories, each resulting in a different maximum mass of neutron stars. Observations and measurements of neutron stars in binary systems can provide information on the properties of neutron stars, for example two heavy neutron stars of roughly two solar masses have been reported in [1] and [2]. Theoretically, the mass and radius of neutron stars can be calculated with the TOV equation, which was established by Tolman, Oppenheimer and Volkoff. Under the assumption of a perfect fluid in gravitational equilibrium ([3] and [4]), the TOV equation can be formulated in many ways, one of them can be found in [5]:

$$\frac{dp(r)}{dr} = -\frac{G}{c^2}\frac{(p(r)+\varepsilon(r))(m(r)+4\pi r^3 p(r)/c^2)}{r^2(1-2Gm(r)/(rc^2))} \tag{1.1}$$

$p(r)$ is the pressure, $\varepsilon(r)$ is the energy density and $m(r)$ is the mass with

$$\frac{dm(r)}{dr} = 4\pi r^2 \frac{\varepsilon(r)}{c^2} \tag{1.2}$$

In order to solve the TOV equation, a relation between for instance between p and ε is needed, which is described as the *Equation of State* (EoS). However, the EoS of neutron stars is still an unresolved issue, since a variety of pressures is predicted under different physical assumptions. This is also displayed in figure 1.1, where several mass-radius curves corresponding to different EoS are shown.

Experimental observations like measuring the masses and radii of neutron stars help to constrain the EoS. The grey lines, for instance, in figure 1.1, can already be ruled out as they do not reach the two solar masses threshold. All colored curves represent an EoS with only non-strange hadronic degrees of freedom. The inclusion of hyperons or kaon condensates usually makes the EoS "softer", which means that the maximum mass decreases. Especially hyperons are expected to be constituents at these high densities because of the fermionic nature of nucleons that makes their chemical potentials a rapidly increasing function of the density $\rho(r)$. When the neutron's chemical potential becomes sufficiently high, the neutrons in the most energetic states on the Fermi surface can decay into hyperons like the Λ or the Ξ via the weak interaction. Figure 1.2 displays these

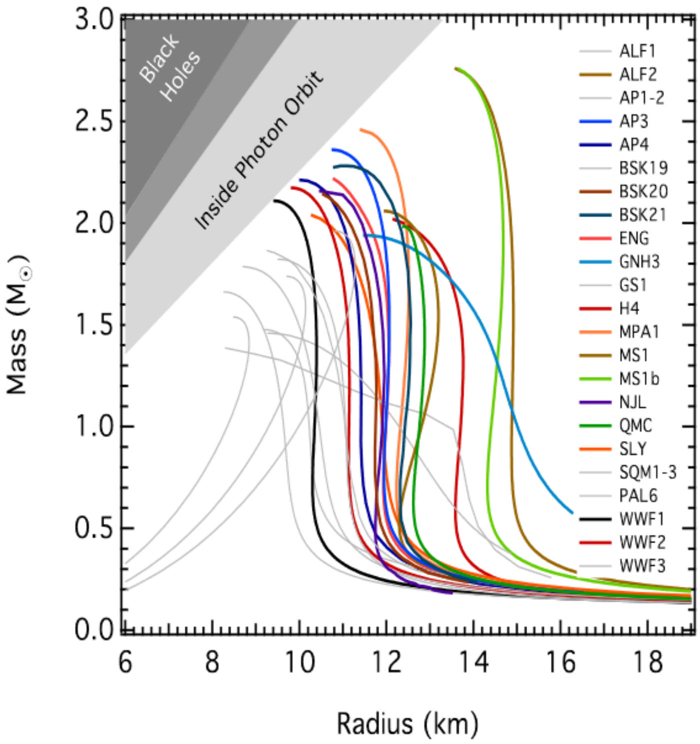

Figure 1.1. Different mass-radius curves corresponding to the equations of state under different physical assumptions ([5]), all of which are yet without the presence of non-nucleonic phases.

chemical potentials. Hyperons are heavier than neutrons which makes them slower, decreasing the pressure and thereby softening the EoS so much that oftentimes the two solar masses cannot be reached anymore.

The theoretical appearance of the hyperons that softens the EoS and decreases the maximal neutron star masses stands opposed to the experimental observations. This is also called the “Hyperon Puzzle”. Three models calculated in a Monte Carlo simulation with different N-Λ interactions were presented in [7] and are shown in figure 1.3. The red curve represents a two-body interaction, the blue and black one three-body interactions. The latter interactions possess a larger repulsion that stiffens the EoS and pushes the curves towards the measurements from [1] and [2]. The difference between the two three-body models is the appearance of Λ hyperons at a different density, which is for the blue curve roughly $0.3\,fm^{-3}$ and for the black line $0.56\,fm^{-3}$. The green curve represents pure neutron matter (PNM) that can reach a maximum mass more than two solar masses, which is in accordance with the nucleonic EoS displayed in figure 1.1.

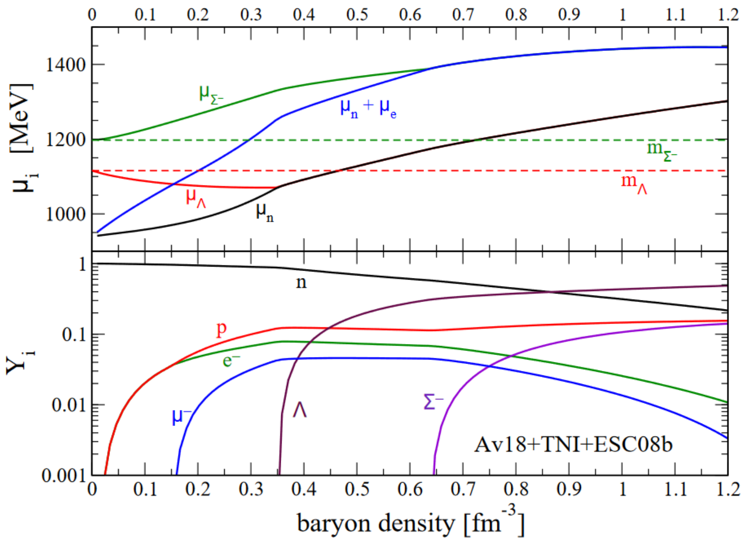

Figure 1.2. This figure is taken from [6]. The upper panel display the chemical potentials μ_i and the lower panel displays the concentrations Y_i of the various stellar constituents as functions of the total baryon density.

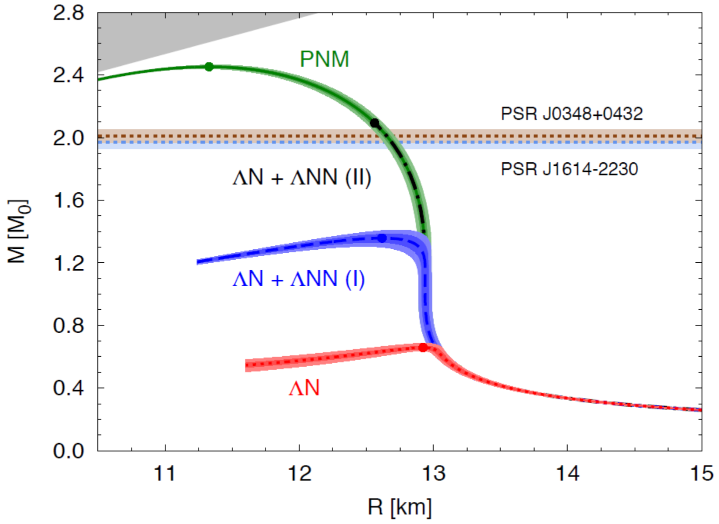

Figure 1.3. The mass-radius relations calculated in a Monte Carlo simulation in [7]. The red curve represents a two-body interaction, while the blue curve and the black dashed line represent three-body interactions. The green line represents pure neutron matter (PNM).

In order to put more precise constraints on the EoS, a deeper understanding of the nucleon-hyperon (N-Y) interactions has to be developed, though. This thesis aims to be a part of this investigation by analyzing the two-body p-Λ interaction and by describing the procedure of generating the Ξ production cross section, which is a vital step for any experimental analysis. The thesis is structured as follows: In the next chapter, the method of femtoscopy will be introduced. With this method, it is possible to analyze the $Y - N$ potential. Subsequently, specifically the p-Λ interaction will be investigated. In chapter 4, the procedure on generating the Ξ production cross section will described. Finally after that, the results will be summarized and a short outlook will be given.

2 Basics of femtoscopy

As discussed in the introduction, the EoS is not yet well established and some of the reasons are the poorly constrained hyperon-nucleon and hyperon-hyperon interaction potentials. The effect of many-body forces can certainly play an important role as well, however the study presented in this thesis concentrates on the two-body interactions. These interactions are studied via the femtoscopy method ([8]). This method provides an alternative to traditional scattering and hypernuclei experiments and was proven to be applicable in small collision systems at LHC energies to study baryon-baryon interactions ([9]).

Femtoscopy is based on building the correlation function between particle pairs produced in collider experiments. The basic idea is that after the hadrons have formed and the system has reached thermal freezeout, i.e. there are no more elastic scattering processes, the produced particles traverse towards the detector undisturbed. However, if two or several particles are emitted close in both momentum and position space they will experience a final state interaction on their way to the detector, which will modify their relative momenta and lead to a correlation signal. As the strong interaction is short-ranged, such modification is expected to occur only if the particles are emitted within few femtometers (1 fm=10^{15} m) from each other. If the particles have small relative momenta they will interact longer and thus produce a stronger correlation signal. Thus femtoscopy is best suited to study particle pairs with low relative momenta k^*. The measurable observable of interest is called the correlation function $C(k^*)$, which has a theoretical definition relating it to the wave-function of the pair, thus making a connection to the interaction potential. The construction of the experimental and theoretical correlation function is discussed in detail in this chapter.

2.1 The correlation function

2.1.1 The theoretical definition

The correlation function $C(\vec{p_1}, \vec{p_2})$ is defined as the ratio between the probability of observing two particles emitted from the source with momenta $\vec{p_1}$ and $\vec{p_2}$, and the probability of observing $\vec{p_1}$ and $\vec{p_2}$ independently of each other ([10]):

$$C(\vec{p_1}, \vec{p_2}) = \frac{P(\vec{p_1}, \vec{p_2})}{P(\vec{p_1}) \cdot P(\vec{p_2})} \tag{2.1}$$

If an interaction is present, $P(\vec{p_1}, \vec{p_2})$ cannot be factorized and consequently, the correlation deviates from unity: $C(\vec{p_1}, \vec{p_2}) \neq 1$.

An equivalent definition relating $C(\vec{p_1}, \vec{p_2})$ to physical quantities is given by the Koonin-Pratt equation as suggested in [8]:

$$C(P,q) = \frac{\int d^4x_a d^4x_b s(p_a,x_a)s(p_b,x_b)|\psi(q,r^*)|^2}{\int d^4x_a s(p_a,x_a)\cdot\int d^4x_b s(p_b,x_b)}. \tag{2.2}$$

Here, $s(p_i,x_i)$ are the single particle source functions ($i=1,2$), which can be seen as the (normalized) probability of emitting particle i with energy and momentum $p_i=(E_i,\vec{p_i})$ at space-time $x_i=(t_i,\vec{x_i})$. $P=p_a+p_b$ is the total and q is the relative 4-momentum vector. Under the assumption that the particles are emitted simultaneously in the center-of-mass system (CMS), $\psi(q,r^*)$ corresponds to the stationary two-particle wave-function. This definition is of particular interest, as it allows to study both the spatial-temporal properties of the collision system (the emission source) and the final state interaction between particle pairs (the wave-function). Equation 2.2 can be simplified by introducing further approximations, as discussed in [8] and [11], leading to:

$$C(\vec{P},\vec{q}) = \int d^3r^*|\psi(\vec{q},\vec{r^*})|^2\int dt^*\mathcal{S}(\vec{r^*}). \tag{2.3}$$

$\mathcal{S}(r^*)$ is the probability density function of the time-dependent relative distance $r^*=x_a-x_b$ and contains the two single particle probability density functions. However, due to statistical limitations in many experiments, it is not possible to make a detailed analysis of the time-behavior of $\mathcal{S}(r^*)$. That is why a static effective source $S(\vec{r^*})$ is used instead. $S(\vec{r^*})$ is the spatial probability density function. It describes the probability of emitting two particles at distance $\vec{r^*}$. Within this thesis, the entire emission and interaction process is assumed to be without any angle dependence and therefore spherically symmetrical. Finally 2.3 can be transformed into

$$C_{theo}(k^*) = \int d^3r^*|\psi(\vec{r^*},\vec{k^*})|^2 S(r^*), \tag{2.4}$$

where $k^*=\frac{1}{2}\cdot|\vec{q}|=\frac{1}{2}\cdot|\vec{p_1}-\vec{p_2}|$ has the property of representing the CM momentum per particle.

A further simplification is the assumption of a static, isotropic Gaussian source, characterized by its width (size) r_0:

$$S_{Gauss}(\vec{r^*}) = (4\pi r_0^2)^{-3/2}\cdot exp\left(-\frac{\vec{r^*}^2}{4r_0^2}\right). \tag{2.5}$$

An example of a Gaussian source with $r_0=1.19$ fm is plotted in figure 2.1.

To demonstrate the properties of the correlation function figure 2.2 shows the p-p $C(k^*)$ assuming different interactions. As expected, regardless of the interaction potential, all correlations converge to unity at high k^*. The green curve represents the case in which all interaction is neglected, but the wave-function is symmetrized to include the effect of the Pauli exclusion principle which is relevant for identical particles. The resulting correlation function is depleted at small k^* and eventually goes to 0.5 for $k^*=0$. Naively one could imagine that this is the case as the protons cannot occupy the same quantum state and consequently the spin alignment of the protons has to be different, thus only half of the spin combinations, corresponding to opposite alignment, are allowed.

The blue curve is the case in which the strong interaction, modeled by the *AV 18* potential [12], is included on top of the quantum statistics. This potential is strongly repulsive on short ranges (until around 0.7 fm) and attractive on intermediate and long ranges. As illustrated in figure 2.2 this leads to a significant enhancement of $C(k^*)$, as most of the particles are emitted at relative distances above 2 fm (see 2.1) and hence are mostly sensitive to the attractive part of the potential.

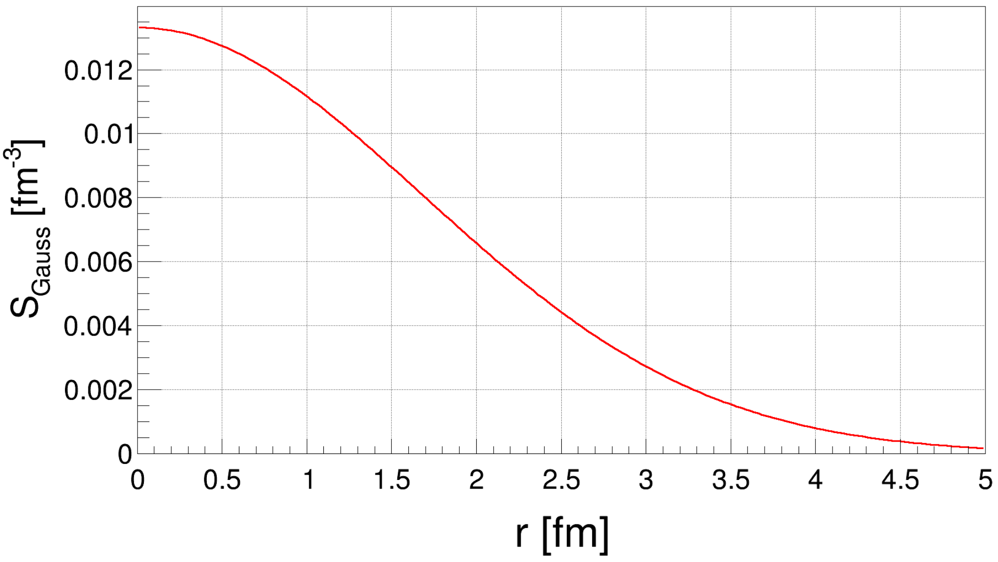

Figure 2.1. The Gaussian source with a width of $r_0 = 1.19\,\mathrm{fm}$.

The mutual attraction causes the protons to be pulled closer to each other, which will in turn reduce their relative momentum.

Finally the red curve adds the Coulomb interaction, which in the case of two protons is purely repulsive, leading to a depletion in the correlation signal at low k^*. The Coulomb potential is $V_{Coulomb} \propto r^{-1}$, whereas V_{strong} declines exponentially, meaning that the former has an effect even at larger r^* ranges leading to a strong repulsion for all particle pairs, and also becomes infinitely repulsive at very low distances. Thus the Coulomb interaction dominates the low k^* region driving the correlation function to a full depletion ($C(k^* = 0) = 0$).

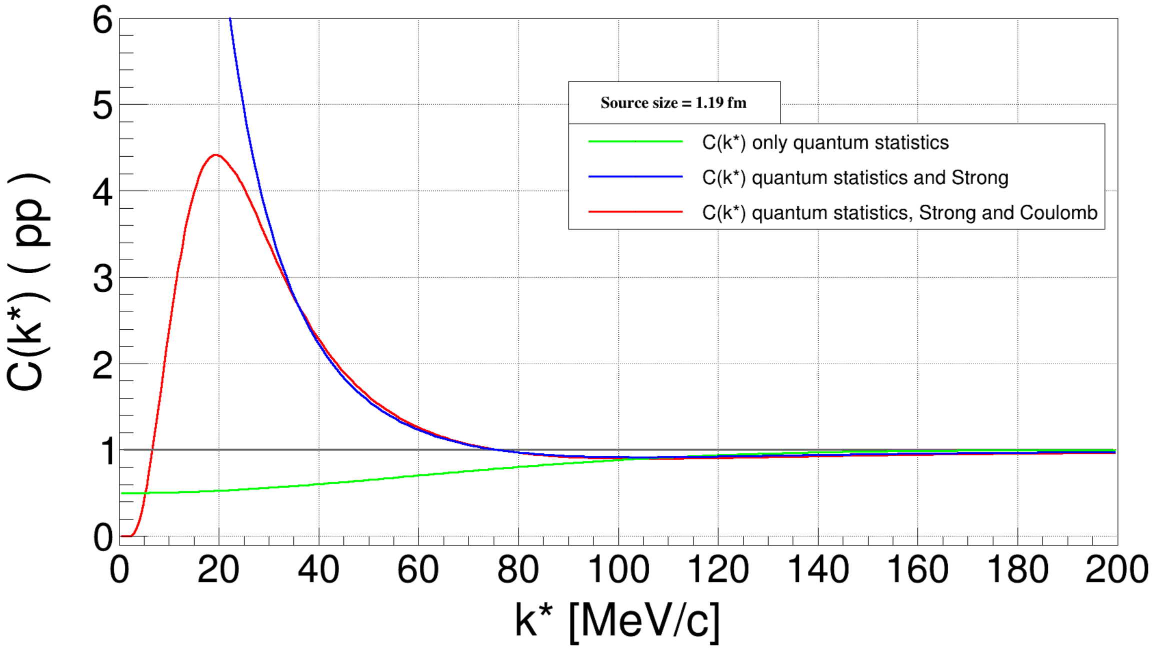

Figure 2.2. These plots display the theoretical correlation functions in a p-p system with source $r_0 = 1.19\,\mathrm{fm}$ for three potential combinations.

2.1.2 The experimental definition

In order to extract the correlation function experimentally an equivalent definition of 2.1 can be derived, which replaces the probabilities with particle yields (N number of pairs). If two particles are emitted in the same event they will be correlated, while particles produced in different (mixed) events will not interact and consequently have no correlation signal. Thus equation 2.1 can be rewritten as

$$C_{exp}(k^*) = \mathcal{N} \frac{N_{same}(k^*)}{N_{mixed}(k^*)}, \tag{2.6}$$

where k^* is the relative momentum between the momenta of both particles in the CMS: $k^* = \frac{1}{2}|\vec{p_1^*} - \vec{p_2^*}|$. The factor $\mathcal{N}$ normalizes the correlation to 1 for $k^* \to \infty$. This condition needs to fulfilled, since particles that are emitted with very large relative momenta are separated very fast and practically no interaction is present, which results in the lack of correlation and $C(k^*) \to 1$.

To illustrate how the experimental correlation function is build an example from p-p collisions at $\sqrt{s} = 13\,\text{TeV}$ collected by the ALICE experiment will be shown. The aim of the current section is to demonstrate the general strategy involved, independent of the detector set up, hence the ALICE experiment will be not be discussed now, but in section 4.2. To build the correlation function it is essential that the detector used is capable of reconstructing the momenta of the particles and to perform particle identification, i.e. determine the species of the detected particles. The other important property to consider is the expected source in the given collision system, as it has a direct consequence on the strength of the correlation signal. As the goal is to investigate the strong interaction between the particles, it is preferable to choose a system with small r_0, as the particles will be emitted close to one another and within the range of the potential. Thus performing femtoscopy in p-p collisions at LHC energies is particularly beneficial ([9]).

The first part of the analysis is to obtain the yields $N_{same}(k^*)$ and $N_{mixed}(k^*)$. This step is detector specific and will not be discussed here. As shown in figure 2.3 usually the same event sample is much more limited in statistics, as the number of pairs in the mixed events can be increased by increasing the number of mixed events used. Due to the different number of pairs in the same and mixed event samples the raw correlation function C_{raw} (see fig. 2.4), which is the ratio of the two samples, is not normalized. The normalization is usually performed at slightly higher k^* region, in which the correlation signal should be converging to unity. In the example shown in fig. 2.4 $C_{raw}(k^*)$ is normalized by fitting it with a constant function in the region $[200, 400]$ MeV. The resulting normalized $C_{exp}(k^*)$ is plotted in 2.5.

2.2 Corrections to the correlation function

The measured correlation function includes several effects that need to be accounted for. The most trivial one is the momentum resolution of the detector, which will smear $C_{exp}(k^*)$. Another detector related effect is the possibility to misidentify a particle and thus study the wrong particle pair. Finally one could have residual correlation signal related to feed-down contributions. These effects will be described shortly in the following, while a detailed discussion on the subject can be found in [13] and [9].

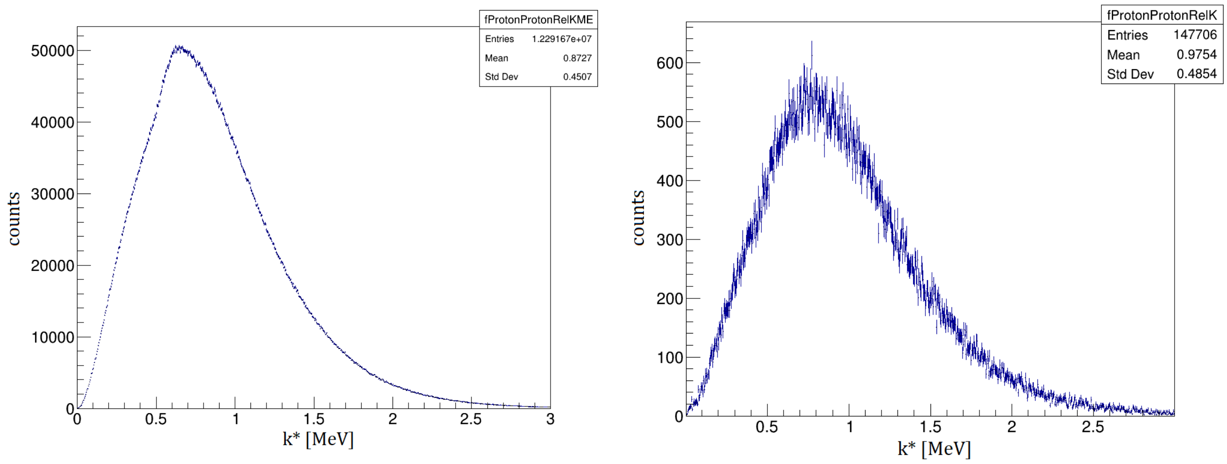

Figure 2.3. The p-p pair production in same events (left) and in mixed events (right). The statistics differ by a factor of approximately 100.

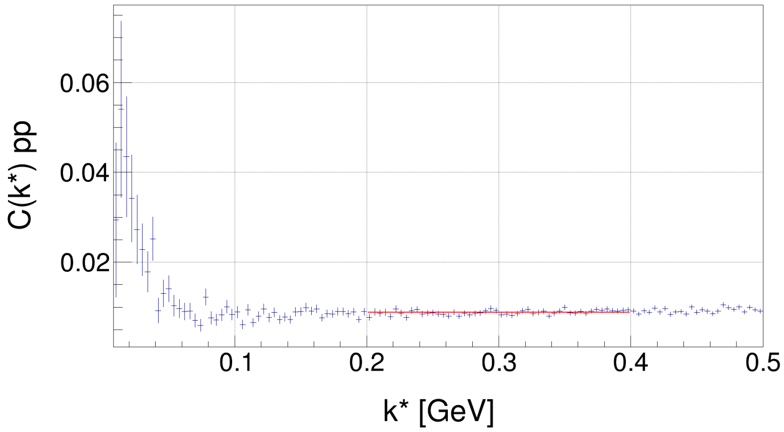

Figure 2.4. C_{raw} for p-p pairs before normalization. The p-p pairs were created in p-p collision at $\sqrt{s} = 13\,\text{TeV}$ at ALICE. The red line represents the constant fit within $200 - 400\,\text{MeV}$.

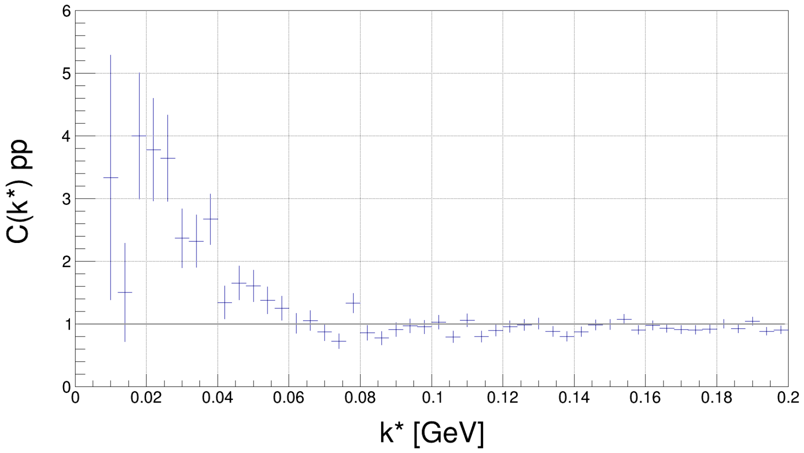

Figure 2.5. C_{exp} for p-p pairs after normalization. The p-p pairs were created in p-p collision at $\sqrt{s} = 13\,\text{TeV}$ at ALICE.

Residuals When the particle pairs are studied, the assumption is that all pairs consist of primary particles created during the collision. However the detectors are typically placed in centimeters or even meters away from the collision point, hence many of the detected particles are not primaries but decay products. The daughters of those decays might be wrongly selected as primary particles and thus carry a residual correlation signal associated with its mother particle. As an example, imagine that one is interested in studying the correlation between particles X and Y, where Y can either be produced in the primary collision or be the decay product of a particle Z. If X and Z are emitted in an event, they will experience a final state interaction. In case Z is long lived it will eventually decay into a Y_Z that will not interact with X anymore and the detector will measure a XY_Z pair which carries the correlation stemming from XZ. Further the measured relative momentum k^* will be different than of the original XZ pairs, as the decay $Z \to Y_Z$ involves certain kinematic topology. For this reason the correlation signal will be modified. The techniques used to correct for those effects are discussed in ([13] and [9]).

Finite momentum resolution Another distortion to the correlation function comes from the finite momentum resolution of the detector. How the detector influences the momenta can be obtained, for example, by running a full-scale Monte Carlo simulations, including both a simulation of the collision and the detector response. This allows to relate the true momentum k^*_{gen} with the reconstructed momentum k^*_{rec}. The correction to the correlation function is applied by multiplying with a momentum smearing matrix.

Impurities Impurities mean misidentifications of particles. In that sense, a pion could be misidentified as a proton, and therefore erroneously contributing to $C(k^*)$. The impurity correction will also is handled similarly as the residuals, although usually it is assumed that the correlation signal associated with impurities is flat ([13], [9]).

2.3 Fitting with the correlation function

It has become clear that the theoretical correlation function $C_{theo}(k^*)$ in equation 2.4 cannot coincide with the experimental correlation function $C_{exp}(k^*)$ in equation 2.6, because of the distortions mentioned above. There are different ways to account for these effects, the strategy currently adopted for the baryon-baryon ALICE analyses in small collision systems follow the prescription presented in [9]. This method applies all corrections onto the theory function and uses data-driven Monte Carlo simulations to evaluate the amount of contributions from feed-down. In essence the total correlation function can be written as

$$C_{total}(k^*) = \sum_{ij} \lambda_{ij} C_{ij}(k^*), \tag{2.7}$$

with

$$\lambda_{i,j}(XY) = \mathcal{P}(X_i) f(X_i) \mathcal{P}(Y_j) f(Y_j), \tag{2.8}$$

where i and j denote the different contributions to X and Y respectively, $\mathcal{P}$ stands for the single particle purity and f is the single particle fraction associated with feed-down from a specific decay channel. $C_{ij}(k^*)$ is the shape of the correlation associated with a specific channel.

The final step in an analysis would be to fit the data using $C_{total}(k^*)$. Nevertheless depending on the analysis there might be additional corrections needed, as e.g. in [9] $C_{total}(k^*)$ is multiplied with a linear base line to take into account possible long-range non-femtoscopy correlations.

2.4 CATS

Throughout this entire thesis, the plots and fits of the correlation function have been made with the help of a program called “Correlation Analysis Tool using the Schrödinger equation” (CATS, [14]). CATS is written in C++ and is designed to numerically compute the theoretical two-particle correlation function from equation 2.4 depending on k^*. Various inputs for the computation must be inserted in order to specify the source and the wave function. For the (Gaussian) source, the source size r_0 has to be defined. Specifying the wave function takes a lot more inputs like the masses and charges, the possible states (singlet, triplet, etc.) of the wave function and the short-range potential that shall be used for the strong interaction (like the Usmani potential ([15]) for pΛ or the AV18 potential for NN). After that, the computation of the integral will be performed numerically, returning a specific C-value for a given k^*-value. Thus, the complete correlation function can be solved and displayed in discrete steps over a predefined range of k^*-bins.

The advantage of CATS over traditional models used in femtoscopy, like the Lednický model [16], is that the numerical solution does not use the effective range expansion and provides an exact solution even for short distances. Additionally there is a lot of flexibility in the choice of the source and potential functions to be used in the computation.

3 pΛ potential variations

In the following section, the N-Y interactions will be investigated. As previously discussed better knowledge on the N-Y interaction is of general interest to describe the EoS and the existence of heavy neutron stars. In particular it is predicted that with increasing nuclear matter density the existence of hyperons becomes energetically favourable compared to neutrons, however their appearance corresponds to a softening of the EoS, which disfavours heavy neutron stars, unless there is additional repulsion acting on the hyperons in dense nuclear matter. As Λ is the lightest hyperon it is the first one to appear in the neutron star, as such the n-Λ will play a major role in the determination of the EoS. Hence it would be of great interest to measure the n-Λ interaction potential, nevertheless neutrons are difficult to detect, specifically the ALICE experiment relies on ionization processes to detect particles, therefore is only sensitive to charged hadrons. However, as Λ is isospin neutral, the p-Λ and n-Λ interactions are alike and analyzing the p-Λ interaction makes it possible to draw conclusions about the n-Λ interaction.

The p-Λ interaction has already been studied by ALICE in [9] (pp collisions at 7 TeV), which reported sensitivity to different potential employing the femtoscopy technique, where the interaction has been modeled by the approximate Lednický model. As the p-Λ potential is on average attractive the correlation function produced by the Lednický model produces only attractive correlation signal, i.e. $C(k^*) > 1$. Nevertheless most of the baryon-baryon potentials, including p-Λ, posses a repulsive core at small radii. The p-Λ correlation function extracted by ALICE (with binning of 20 MeV in k^*) is plotted in figure 3.1.
In this figure there is a visible dip below unity for k^* values larger than 100 MeV. In [9] this depletion is associated with a linear baseline used to model non-femtoscopy correlations. However in this work we would like to discuss the possibility for an alternative explanation, namely that this depletion is a direct consequence of the repulsive core of the potential.
This effect cannot be studied with the Lednický model, as it only works with the asymptotic solution of the wave-function and is not sensitive to the repulsive part of the potential. An alternative approach is to use a local potential, which includes a repulsive core, and use CATS to study $C(k^*)$. A commonly used model for the p-Λ interaction is the Usmani potential [15], which includes a phenomenological repulsive core. In this chapter we use the Usmani potential as the base for a toy-model, with which we attempt to describe the ALICE data without the inclusion of a non-femtoscopic baseline, only by fine-tuning the phenomenological repulsive core of the potential. As described in the previous section, in order to analyze the ALICE data, one must perform a fit with the function $C_{total}(k^*)$ that contains the theoretical $C_{p\Lambda,theo.}$ and possible residual correlations.
In [9] and [13] the residual correlations are treated in detail, but it is also shown that they produce an approximately flat correlation signal, thus in the current analysis we use the fraction of primary signal as obtained by ALICE ($\lambda_{theo} = 47\%$), but assume that the feed-down and misidentified pairs produce correlation equal to unity. Further in [13] one could see that effect of momentum resolution is negligible for the p-Λ correlation, hence it is neglected in the current study. With the above simplifications $C_{total}(k^*)$ from equation 2.7 turns into the following fit function:

$$C_{fit}(k^*) = N \cdot \left(\lambda_{theo} C_{theo}(k^*) + (1 - \lambda_{theo})\right), \tag{3.1}$$

where N is a constant normalization parameter to be determined by the fit and $\lambda_{theo} = 0.47$. The most important constituent within this fit is C_{theo}. According to equation 2.4, it is defined as

$$C_{theo}(k^*) = \int d^3r^* |\psi(\vec{r^*}, k^*)|^2 S(\vec{r^*}) \tag{3.2}$$

For the p-Λ correlation in the Run 1 data set, the source is assumed to be Gaussian with width of $r_0 = 1.144\,\mathrm{fm}$ ([9]). The wave function ψ contains the most interesting quantity, which is the p-Λ potential. The two-particle wave function ψ is computed using the Usmani potential.

Note that if the correlation is fitted using equation 3.1 and the default Usmani potential the data cannot be properly described (fig. 3.1). This discrepancy is the motivation for a detailed investigation of the interaction between the proton and the Λ.

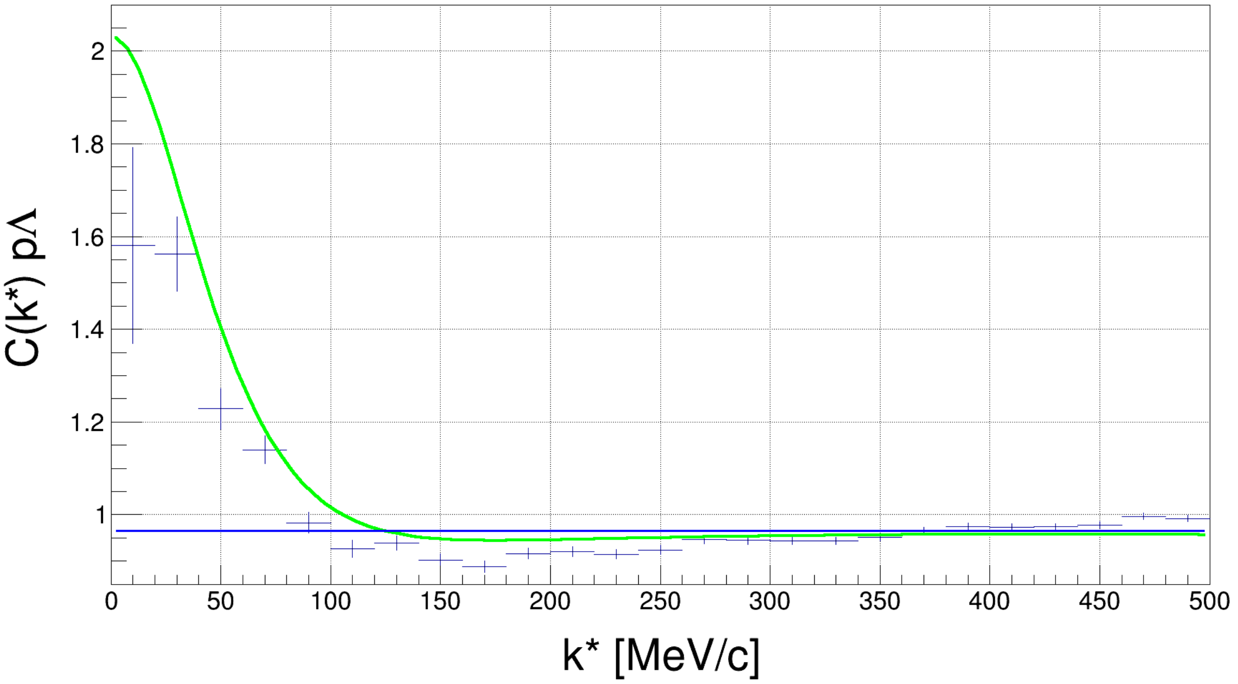

Figure 3.1. The ALICE data set from Run 1 in 2010 and the correlation function including the Usmani potential.

3.1 The Usmani potential

The Usmani potential describes the p-Λ potential and can be seen in figure 3.2. The wave function is built for two fermions, meaning that only spin states $S = 0$ and $S = 1$ are allowed. Here, only the singlet ($1S0$) and triplet ($3S1$) states are shown, as all other waves with angular momentum $l \geq 1$ are assumed to have negligible influence on the correlation function at low k^*. In [15], the formula of the Usmani potential is given:

$$V_{Usmani} = V_C - \left(\overline{V} - \frac{1}{4} V_\sigma \vec{\sigma}_\Lambda \cdot \vec{\sigma}_p \right) T_\pi^2, \tag{3.3}$$

where T_π describes the one-pion exchange (OPE) tensor potential, $\overline{V}$ is the spin-independent part of the attractive potential, while the repulsive spin interaction between the two fermions is covered by V_σ. All of these components posses a real physics definition, however, the biggest contribution to the short range behavior is determined by the *repulsive core* V_C:

$$V_C = W_C \left(1 + exp\left(\frac{r-R}{d}\right)\right)^{-1}, \tag{3.4}$$

with $W_C = 2137\,\mathrm{MeV}$, $R = 0.5\,\mathrm{fm}$ and $d = 0.2\,\mathrm{fm}$, which is just an effective parameterization. The parameters in equation 3.4 are determined based on a fit to the available scattering data (e.g. [17]–[19]).

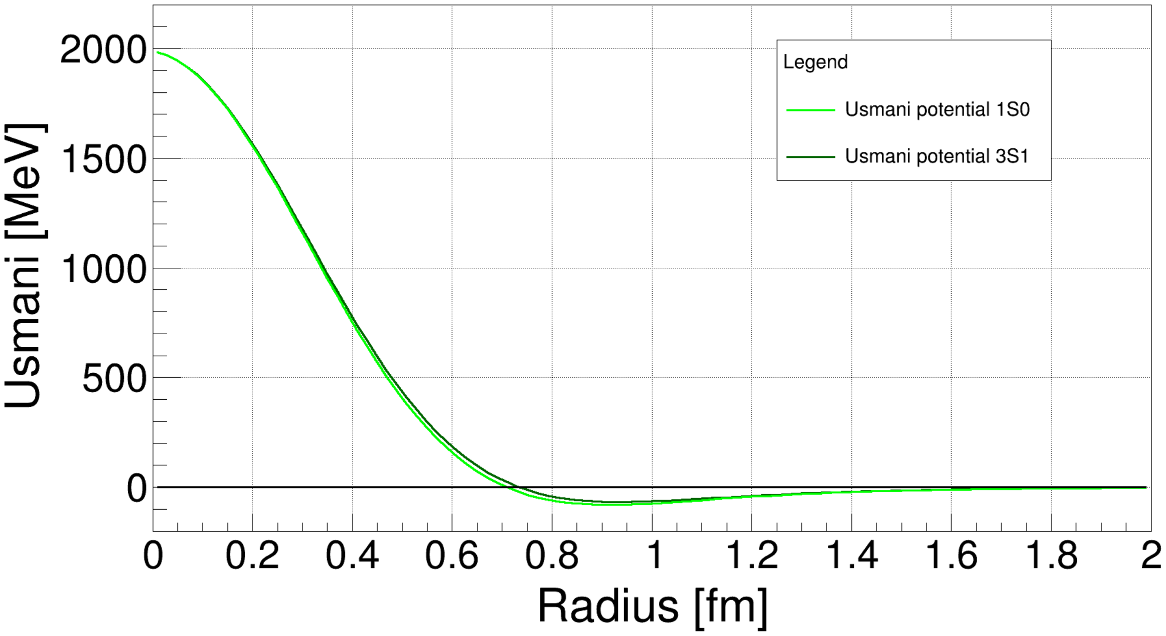

Figure 3.2. This figure displays the Usmani potential for the $1S0$ and $3S1$ waves.

Note that a potential cannot be directly measured, but rather its properties can be studied via the scattering parameters. A detailed description of that can be found in [20]. In summary, analyzing the differential cross section of the outgoing spherical wave leads to determining the phase shift $\delta_l(k)$ between the scattered and the unscattered wave depending on the wave number k and the angular momentum l. Under the assumption of low energy scattering, in which the $S-$waves dominate ($l = 0$), $\delta_0(k)$ can be expanded with the help of the so-called *effective range expansion* in the form of:

$$\lim_{k\to 0} k \cdot \cot\delta_0(k) = -\frac{1}{a} + \frac{1}{2} r_{eff} \cdot k^2, \tag{3.5}$$

where a is called the *scattering length* and r_{eff} the *effective range*. These two parameters are characteristic for any two-body potential. An attractive interaction potential corresponds to negative a, and its absolute value is related to the strength of the interaction. r_{eff} is related to the range of the potential. The Usmani potential in particular delivers $a = -2.88\,\mathrm{fm}$ and $r_{eff} = 2.92\,\mathrm{fm}$ for the singlet state, and $a = -1.66\,\mathrm{fm}$ and $r_{eff} = 3.78\,\mathrm{fm}$ for the triplet state ([15]) and clearly points to a strongly attractive interaction.

To go back to the original problem, figure 3.1 displays the discrepancy between the experimental data and the shape of the theoretical fit that uses the Usmani potential. The Usmani potential describes the scattering data very well, nevertheless as these data are located at $k^* > 60$ MeV, they are mostly sensitive to the scattering length a and effective range r_{eff}. The question we would like to address is if the same (or similar) scattering parameters can be obtained by different choice of parameters W_C, R and d for the repulsive core. As the scattering parameters are only sensitive to the long-range asymptotic behaviour of the potential and not to the shape of the repulsive core, there might be room for improvement by investigating the sensitivity of $C(k^*)$ to the short-range part of the potential. Therefore what will be attempted in the following section are small adjustments to the repulsive core. The three parameters W_C, R and d will be varied, so that the shape of the correlation fit changes, but still produces similar scattering parameters. The ultimate goal is to to describe the femtoscopy data, whilst preserving the known properties of the p-Λ interaction.

3.2 Usmani potential variations

Before presenting the results of these Usmani potential variations, the approach will be explained shortly. To use the data points from ALICE from Run 1 with a source size of 1.144 fm, they are inserted into a ROOT histogram. The theoretical correlation function C_{theo} of the primary pair is computed with CATS by numerically solving the Schrodinger equation. The fit function C_{fit} is defined and passed to the ROOT fitter *Fit* ([21]), which than fits the data points in the histogram. The parameters within C_{fit} can be chosen to be fixed or free. If free, their values are determined by the fitting procure, based on a minimization of the deviation between C_{fit} and the data points. The goal is to change the potential parameters W_C, R and d in the repulsive core V_C of the Usmani potential in order to describe the data points, while producing the same scattering parameters a and r_{eff} of the Usmani potential. Finally the normalization constant N is treated as a free parameter, while the λ_{theo} parameter fixed from [9]. As many different parameters W_C, R and d combinations have been tried out, only a selection of results will be shown here.

The best result After performing an extensive scan over different combinations of W_C, R and d, it was determined that it is possible to find many variations resulting in similar scattering parameters, however all of them produce extremely similar correlation functions. Figure 3.3 shows an example of that, by comparing the original correlation (green curve) with the one obtained by modifying the repulsive core such as to obtain "the best" scattering parameters, i.e. deviating as little as possible from the original values. The modification of the repulsive core consists of an increase of W_C by 1% and d by 5%, and a decrease of R by 5%. The red curve in figure 3.4, shows that this V_C variation maintains the overall shape of the potential.

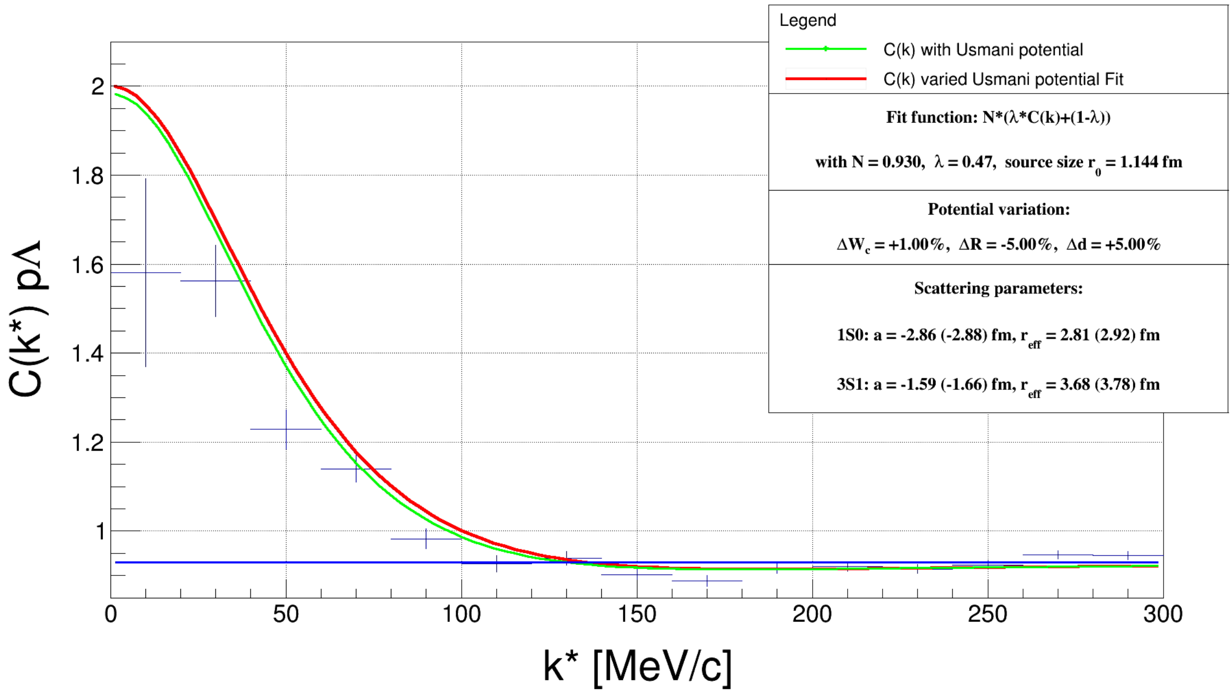

Figure 3.3. The best result for the variation of the repulsive core V_C with $\Delta W_C = +1\%$, $\Delta R = -5\%$ and $\Delta d = +5\%$.

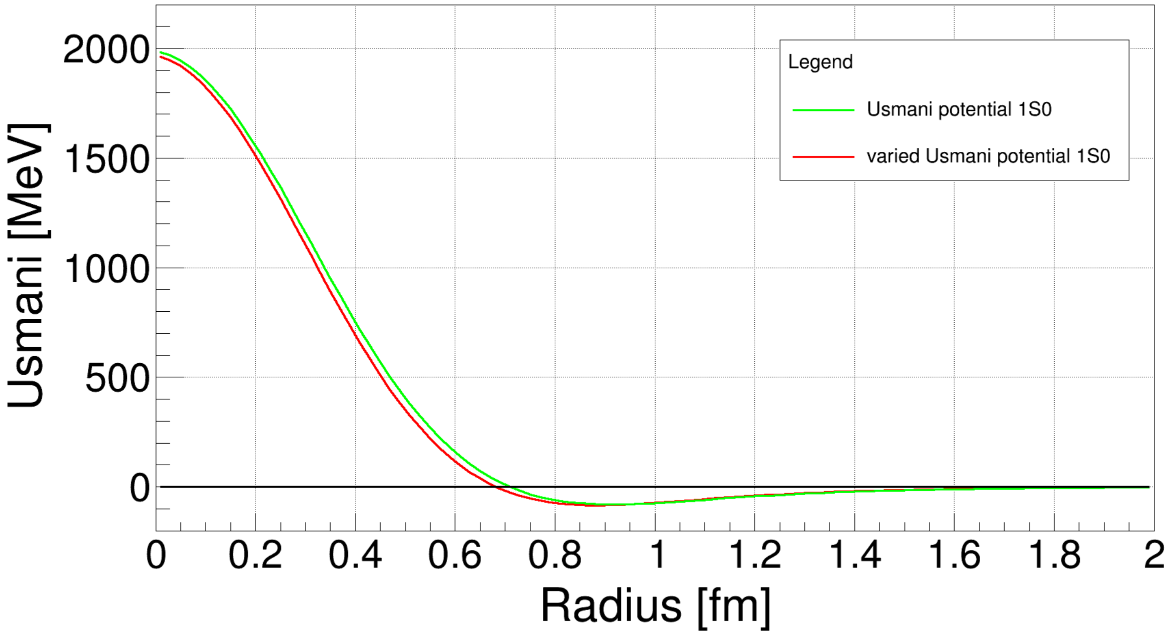

Figure 3.4. The varied Usmani potential for the $1S0$ wave with $\Delta W_C = +1\%$, $R = -5\%$ and $d = +5\%$ compared to the normal Usmani potential.

This result shows that the shape of the experimental data points cannot be reproduced by slight potential variations, because neither the enhanced dip at around 170 MeV nor the linear slope are adopted by the red fit. It seems that the correlation function is primarily sensitive to the scattering parameters and the exact shape of the potential is less important. Hence we conclude that the data cannot be properly described without the inclusion of the linear non-femtoscopic background correlations.

The free fit To illustrate even further that the fit cannot take the same shape as the data, another potential variation can be seen in figure 3.5. Here, the red fit contains only free parameters, namely W_C, R, d and N, which means in turn that the resulting scattering parameters are incompatible with the scattering data. However, even with maximal freedom, the observed dip in the correlation function around $k^* = 170$ MeV is still not reproduced. While figure 3.5 suggests that the free fit provides a much better overall description of the data compared to the original Usmani potential, this is in fact misleading, as the non-femtoscopic baseline is intentionally not included in the fit. The inclusion of such baseline results in a perfect fit in the whole k^* region, as demonstrated in [9].

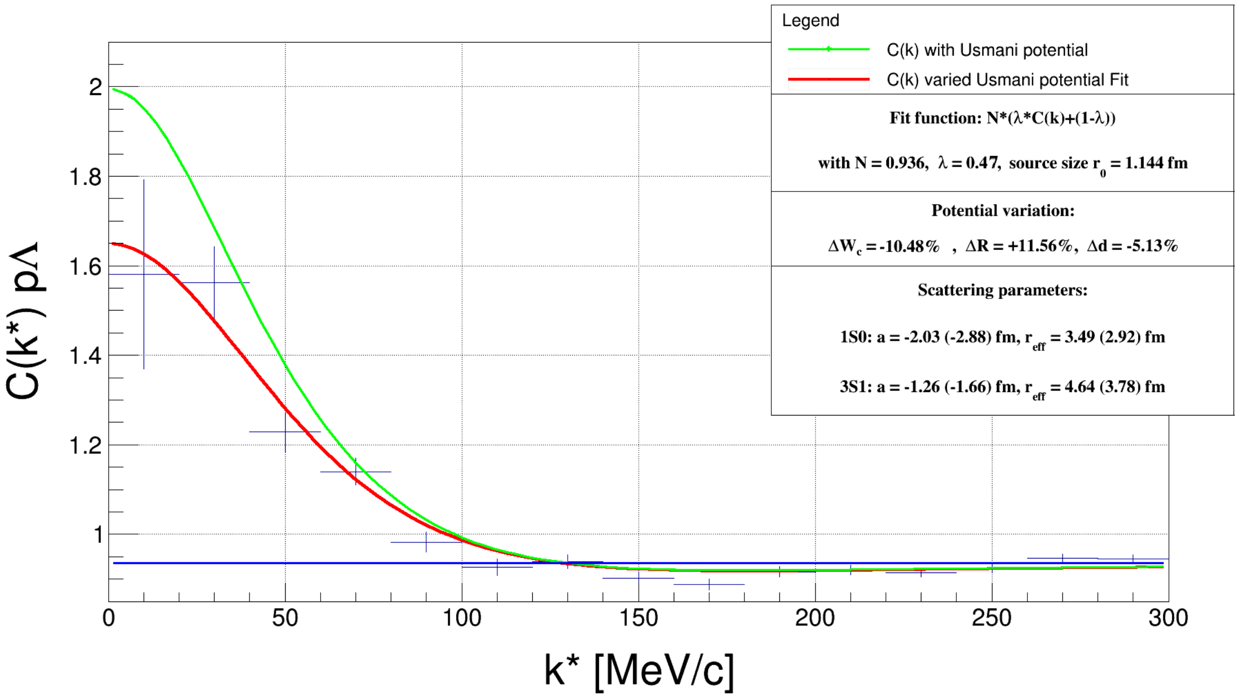

Figure 3.5. The potential variation with several free parameters.

3.2.1 Conclusion on the pΛ potential variations

The p-Λ correlation function measured by ALICE in pp collisions at 7 TeV is analyzed in [9], assuming a linear non-femtoscopic background to account for the observed raising behaviour of $C(k^*)$ at $k^* > 150$ MeV. We attempted to refit the data without the inclusion of such baseline, and instead modify the repulsive core of the Usmani potential. This study revealed that the potential and the resulting correlation function cannot be significantly modified without changing the scattering parameters to unrealistic values, and even in this case the ALICE data cannot be properly fitted. This is a clear indication that the observed effect in the correlation function is not a property of the potential. Thus, as discussed in [9], a linear baseline is needed to account for those non-femtoscopy effects, which are at the moment of unknown origin. Possible explanations may be related either to conservation laws [22], or may be related to the production and emission mechanism of particles. The latter is discussed in [23], where the same data set is analyzed using angular correlations between particle pairs, which reveal strong correlation signal as a function of $\Delta\varphi - \Delta\eta$. These effects are not properly modeled by Monte-Carlo simulations and as such difficult to study.

4 Ξ^- production analysis

4.1 $p\Xi$ lattice potentials

The Λ is the lightest hyperon, nevertheless in the context of neutron stars also heavier hyperons, like the Ξ or Ω, may play in important role. The reason is that with increasing nuclear density even the production of heavier particles can become energetically favorable. This will result in further degrees of freedom and softening of the EoS. As already discussed, this prohibits the existence of heavy neutron stars, which contradicts with experimental observations. In [24] the authors present results highlighting that introduction of repulsive a n-Ξ^- potential hardens the equation of state, allowing the existence of heavier neutron stars. This is demonstrated in figure 4.1, taken from [24], as the different lines correspond to different values of the in-medium potential U_Ξ and clearly large repulsive (positive) values can describe 2-solar mass neutron stars.

Further in [25] a lattice QCD calculation predicts that the n-Ξ^- is repulsive, nevertheless this is experimentally unobserved. Unfortunately the n-Ξ^- correlation function is unlikely to be measured, as it demands the detection and particle identification of both charged and uncharged particles and there is currently no experiment capable of performing this type of reconstruction with sufficient statistics. Thus only an indirect study of the n-Ξ^- interaction is feasible, using a similar isospin channel. The neutron and Ξ^- have both total isospin $I = 1/2$ and third component $I_3 = -1/2$, hence the n-Ξ^- has only $I = 1$ and $I_3 = -1$. On the other hand both the proton and Ξ^0 have $I = 1/2$ and $I_3 = 1/2$, hence the p-Ξ^0 interaction has only the configuration $I = 1$ and $I_3 = 1$. The relevant input parameter for the lattice calculation is I, hence the n-Ξ^- and p-Ξ^0 cases are identical and for this reason the p-Ξ^0 interaction is the best experimental probe in the context of neutron stars. However a complication arises as the Ξ^0 decays into a $\Lambda\pi^0$ and finally the $\pi^0 \to \gamma\gamma$. The detection of photons is possible with the ALICE detector, but the reconstruction the Ξ^0 becomes highly inefficient and contaminated with combinatorial background, making any analysis extremely challenging.

Even the latest Run 2 ALICE data will be insufficient for a detailed study of this system, hence an alternative way of probing the n-Ξ^- interaction is needed. The best experimental option is to study the p-Ξ^-, as the Ξ^- is reconstructed from the decay scheme $\Xi^- \to \Lambda\pi^- \to \pi^+\pi^-\pi^-$, i.e. the final state consists entirely of charged pions, which are very easy to detect. A complication comes from the theoretical side, as the proton and the Ξ^- have opposite sign of I_3, which leads to two possible configuration for the isospin of the pair: $(I, I_3) = (1, 0)$ or $(I, I_3) = (0, 0)$ and hence measuring the p-Ξ^- interaction cannot disentangle between the two cases. The lattice potential from [25] gives predictions for all possible isospin configurations of the N-Ξ interaction, hence the p-Ξ^- correlation function can be computed based on this model. If the lattice calculations can describe the p-Ξ^- interaction this would be a strong hint that the model is correct and consequently the n-Ξ^- potential repulsive. It should be stressed that such conclusions would be highly model-dependent, as e.g. it can happen that the model overshoots the repulsion in the $I = 1$ channel and the attractiveness of the $I = 0$ channel, leading to good fit of the p-Ξ^- data, but yet wrong description of the n-Ξ^-.

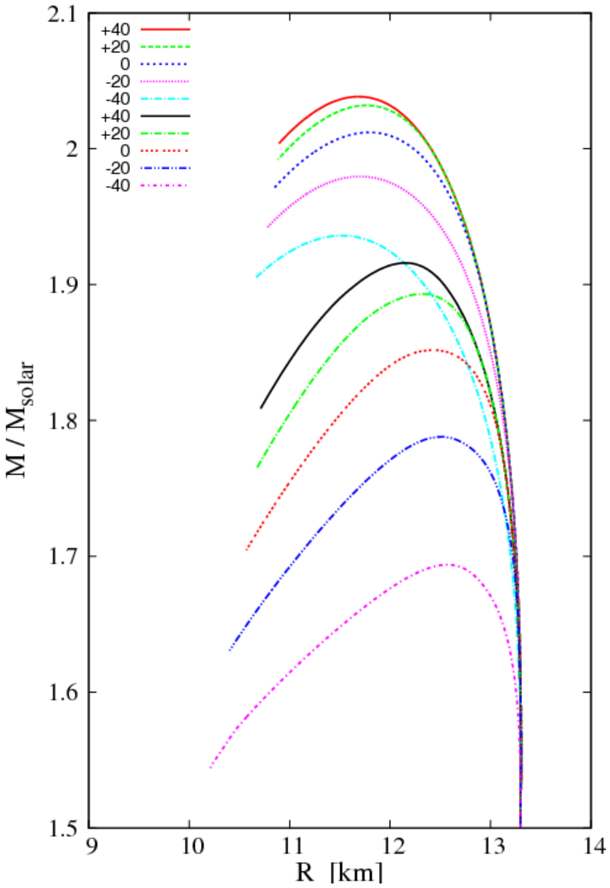

Figure 4.1. Mass-radius relation for the neutron stars, obtained for different $U_{\Xi}^{(N)}$ potential and computing the resulting EoS. The main message of this picture is that increasing the repulsiveness of the in-medium $U_{\Xi}^{(N)}$ potential to values of up to 40 MeV leads to EoS capable of reproducing neutron stars of 2 solar masses. This figure originates from [24].

Nevertheless a measurement of the p-Ξ^- correlation would be the first experimental result capable of investigating the N-Ξ interaction and relating it to the equation of state, hence it is of great interest to perform.

One of the goals of this bachelor thesis, presented in this chapter, is to investigate the Ξ^- production in ALICE in pp collisions at 13 TeV, in preparation for the upcoming femtoscopy analysis of the p-Ξ^- interaction. Of primary interest is to quantify the amount of Ξ^- particles measured and test if the default cuts planned to be used in the femtoscopy analysis are efficient. As a complementary study the Ξ^- yield will be corrected for acceptance and efficiency and the total production cross section within the ALICE geometric acceptance will be computed.

4.2 Experimental setup

4.2.1 The ALICE detector

The ALICE (A Large Ion Collider Experiment) detector is a heavy-ion detector located at the LHC at CERN, focusing on the strong interaction in heavy nuclei collisions when temperature and density reach extreme values up to the production of quark-gluon plasma. Thereby, it allows an extensive study of all particles produced in such collisions, such as hadrons, photons, electrons and muons.

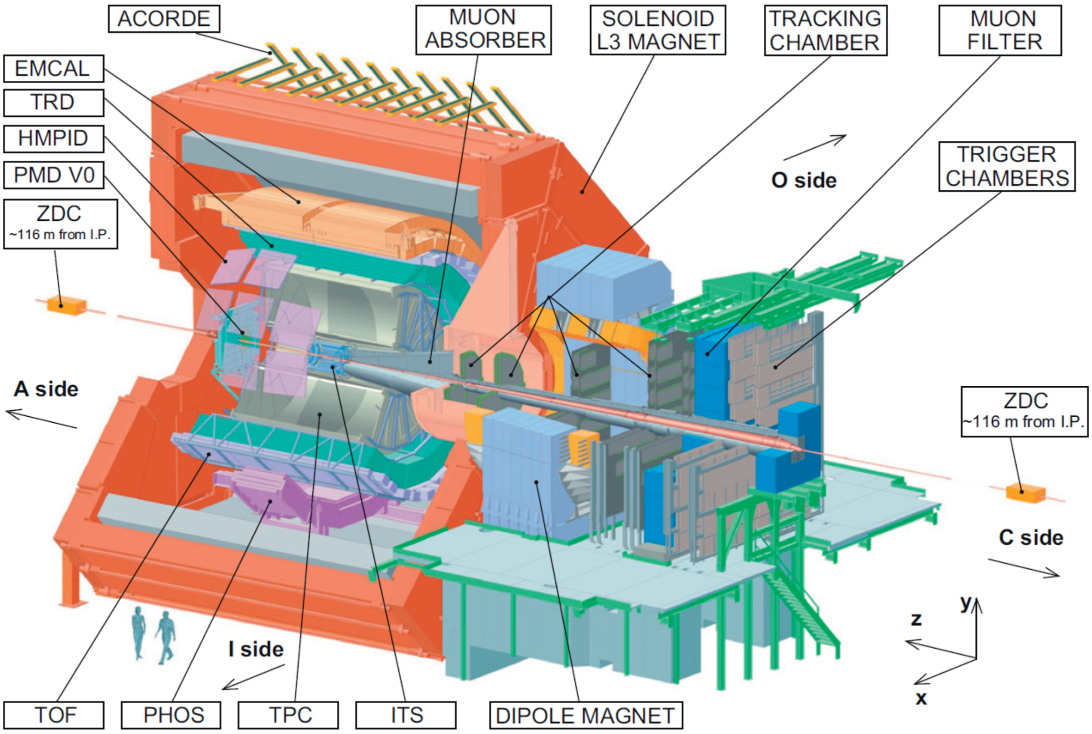

Figure 4.2. The schematic overview of the ALICE detector and its labeled inner components [26].

The structure and inner components of the ALICE detector can be seen in figure 4.2 and will be shortly described in the following. For a more detailed description, [27] should be considered.

The z-axis of the ALICE detector coordinate system is aligned with the beam axis, whereas the x-y-plane is oriented perpendicularly to the beam and z-axis. The ALICE detector system consists of a central barrel and a forward muon spectrometer. The barrel detectors are used to measure hadrons, electrons and photons, covering polar angles from 45^o to 135^o. These central detectors are surrounded by a large solenoid magnet with a magnetic field of $B = 0.5\,T$ parallel to the beam direction.

The central barrel detectors are used for measuring the scattered particles. From the inside out, the barrel includes the Inner Tracking System (ITS), which consists of six planes of high-resolution detectors. The ITS is embedded in the cylindrical Time Projection Chamber (TPC), which is surrounded by the Time-of-Flight (TOF) detector. All these detectors possess full azimuthal coverage. Further detectors beyond the TOF detector are the Ring Cherenkov (HMPID) and Transition Radiation (TRD) detectors and two electromagnetic calorimeters (PHOS and EMCal). Furthermore, there are some smaller detectors (ZDC, PMD, FMD, T0, V0) located at small polar angles for event characterization and triggering. This thesis focusses on tracking and particle identification (PID), meaning that the analysis is predominantly based on the ITS, TPC and TOF detectors, which will be described in further detail in the following sections.

4.2.1.1 The ITS

The Inner Tracking System (ITS) is the detector closest to the beam pipe. Its main goals are to provide a precise primary vertex, reconstruct secondary vertices, identify particles with low momenta ($< 200\,\mathrm{MeV}$), improve the momentum and angle resolution for particles reconstructed in the TPC and reconstruct particles traversing the dead regions of the TPC [27].

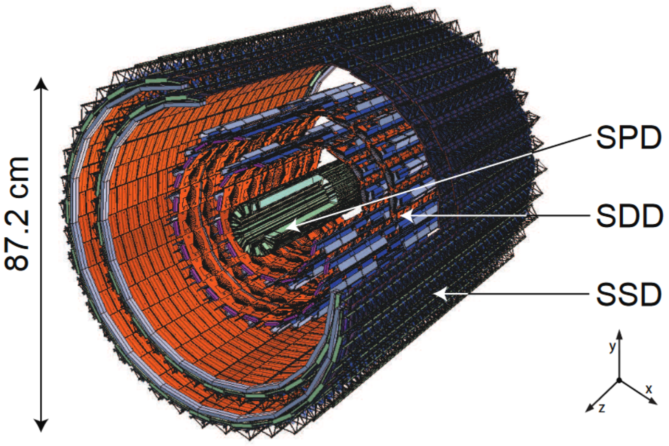

Figure 4.3. Layout and inner structure of the ITS [28], together with the ALICE coordinate system.

Figure 4.3 displays a schematic of the ITS. It consists of six planes of high-resolution silicon detectors. The two innermost layers are silicon pixel detectors (SPD), the two intermediate layers are silicon drift detectors (SDD), and the two outmost layers are silicon strip detectors (SSD). Through combining the measured tracks in each of these planes and matching them to the TPC tracks, primary and secondary vertices can precisely be reconstructed with a resolution of less than 100 μm [28].

4.2.1.2 The TPC

With the Time Projection Chamber (TPC), it is possible to reconstruct the trajectories of traversing charged particles and determine their momentum by measuring their bending radius within the magnetic field. At the same time, it is also possible to measure the energy loss of these particles. By combining momentum and energy loss, it is possible to identify each particle. In the following, a short summary will be given about the structure and the working principle of the TPC. For a more detailed description, [26] should be considered.

The TPC is a hollow cylinder surrounding the ITS with an inner radius of roughly 85 cm and an outer radius of about 250 cm, as it is displayed in figure 4.4. This volume is filled with a counting gas (Ne (85.7%), CO2 (9.5%), N2 (4.8%)) at atmospheric pressure and contains an axial electrostatic field (or ‘drift field’) of 400 V/cm between the central conducting electrode charged with 100 kV and the two end caps. The TPC is coaxial to ITS and beam, parallel to the detector’s solenoid magnetic field and covers a pseudorapidity of $|\eta| < 0.9$.

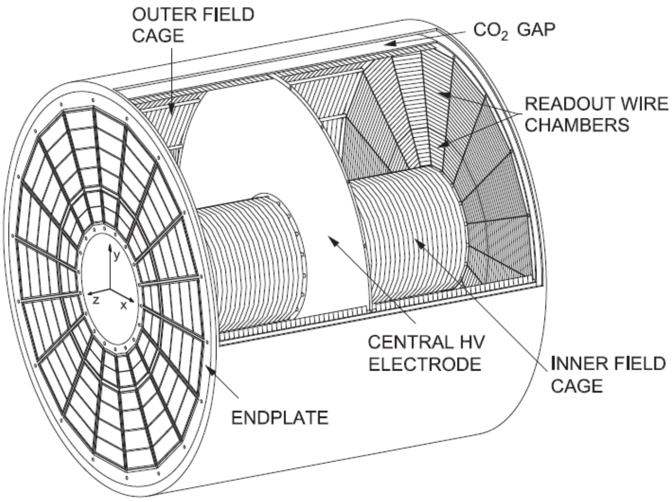

Figure 4.4. 3D view of the TPC [26].

As a charged particle traverses the hollow, gas-filled cylinder, it ionizes the gas, creating pairs of electrons and ions along its track. Because of the opposite charges of electron and ion, the electric field separates the two particles, causing the electrons to drift towards the readout chambers at the end caps. However, the signal induced on these electrodes by the electrons would still be unmeasurable by modern electronics. That is why the electron signal has to be amplified, which is done with the help of Multi-Wire Proportional Chambers (MWPC). The working principle of the MWPC is applying a high voltage to an array of wires (as anodes) in front of the readout pads on ground potential (as cathodes). That way, the electrons are accelerated towards the wires, ionizing the gas again nearby the wires and thereby simultaneously generating an electron avalanche. These avalanche electrons are predominantly measured at the nearest wire in form of a pulse, which causes a high spatial resolution of the primary electron that was set free when the original, traversing particle ionized the gas. Therefore, the track of that particle can be reconstructed as well.

Measuring the time and space of the single ionization events leads to finding out the bending radius of the original particle caused by the effect of the magnetic field. With that bending radius, the momentum of the traversing particle can be determined. Furthermore, through the interaction with the gas and the resulting electron-ion pair generation, the traversing particle loses parts of its initial energy. The number of created electron-ion pairs depends on its energy loss and therefore, this energy loss can be measured. Obviously, how much energy is lost along the way depends on different properties of the particle itself and on the gas. The mean energy loss of a traversing particle can be described by the famous Bethe-Bloch formula:

$$-\left\langle \frac{dE}{dx} \right\rangle = \frac{4\pi n_e z^2}{m_e c^2 \beta^2} \cdot \left(\frac{e^2}{4\pi\varepsilon_0}\right)^2 \cdot \left[ln\left(\frac{2m_e c^2\beta^2}{I\cdot(1-\beta^2)}\right) - \beta^2\right] \tag{4.1}$$

The relevant properties of the particle are its velocity ($\beta = v/c$) and its charge (z), properties of the medium are the electron density (n_e) and the average excitation potential (I). If the velocity β is replaced with the momentum, a mass dependence can be created, and the particles can be identified. Figure 4.5 shows an energy loss measurement depending on the momenta of various particles in a Pb-Pb collision.

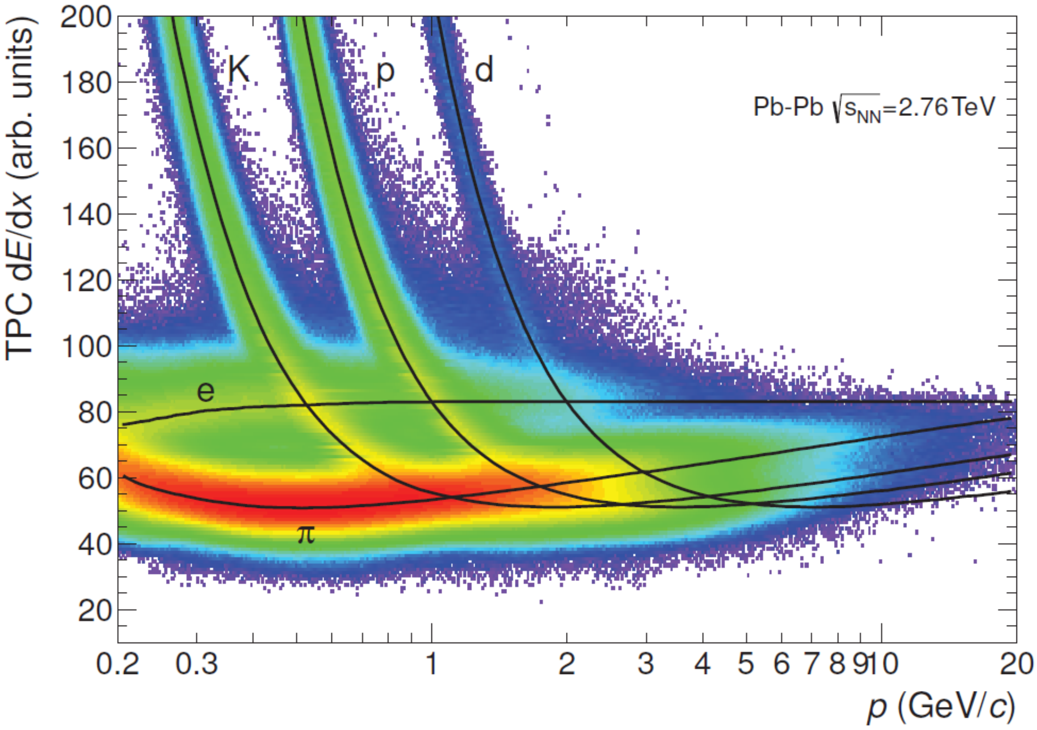

Figure 4.5. This histogram displays the energy loss versus momentum in a Pb-Pb collision at $\sqrt{s} = 2.76$ TeV at ALICE [29].

It becomes quite clear that the different bands can be distinguished for momenta $p < 1$ GeV. Above that threshold, the bands start to overlap and additional information is needed for particle identification, for instance with the help of the TOF detector.

4.2.1.3 The TOF detector

The purpose of the Time-Of-Flight (TOF) detector is, as the name suggests, measuring the time of flight of the particles between the collision and the TOF detection. The technical details can be taken from [27], however a short description will be presented in this section. The TOF detector consists of multiple Multigap Resistive Plate Chambers (MRPC). Thereby, the detector is subdivided into 18 supermodules, which can be seen in in figure 4.6. Just like the TPC, this technology is also based on gas ionization by a traversing charged particle causing an electron avalanche, which generates a signal on the respective electrodes. The TOF surrounds the TPC with an inner radius of 370 cm and an outer radius of 399 cm and also covers a pseudorapidity of $|\eta < 0.9|$. The T0 detector, which includes two Cherenkov counters, provides the start time for the measurement. The overall time resolution can vary, depending on the particles (e.g. pions, kaons) and type of collision (e.g. p-p, Pb-Pb), but lies in between 20 and 100 ps [29].

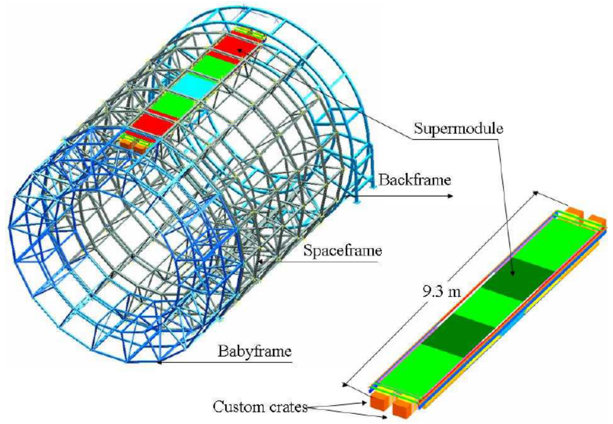

Figure 4.6. The raw structure of the TOF with 18 supermodules from [27]. Each supermodule contains 5 modules.

By measuring the time of flight, particles can also be identified. The TOF can be used for particle identification in intermediate momentum ranges (up to 2.5 GeV for pions and kaons and up to 4 GeV for protons [29]) and therefore extends the sphere of action of the TPC. However, tracks with a very low momentum ($p < 0.3\,\text{GeV}$) are not able to reach the TOF since the bending effect of the magnetic field is too strong, and the particles curl and stay within the TPC volume. When the time of flight is measured, the velocity can easily be calculated because the distance is also known. With this velocity v and the measured momentum p in the TPC, the (rest) mass m_0 can be determined, and thereby the particle can be identified:

$$p = m_0 \gamma v \tag{4.2}$$

Here, γ is the Loretz factor: $\gamma = \frac{1}{\sqrt{1-\beta^2}}$.

In figure 4.7, the momentum and the velocity (as $\beta = v/c$) of charged particles are plotted in a Pb-Pb collision. The different bands represent different particles and are clearly distinguishable from each other. As one would suspect, the electrons and the pions travel nearly at the speed of light, whereas the deuterons are the slowest particles.

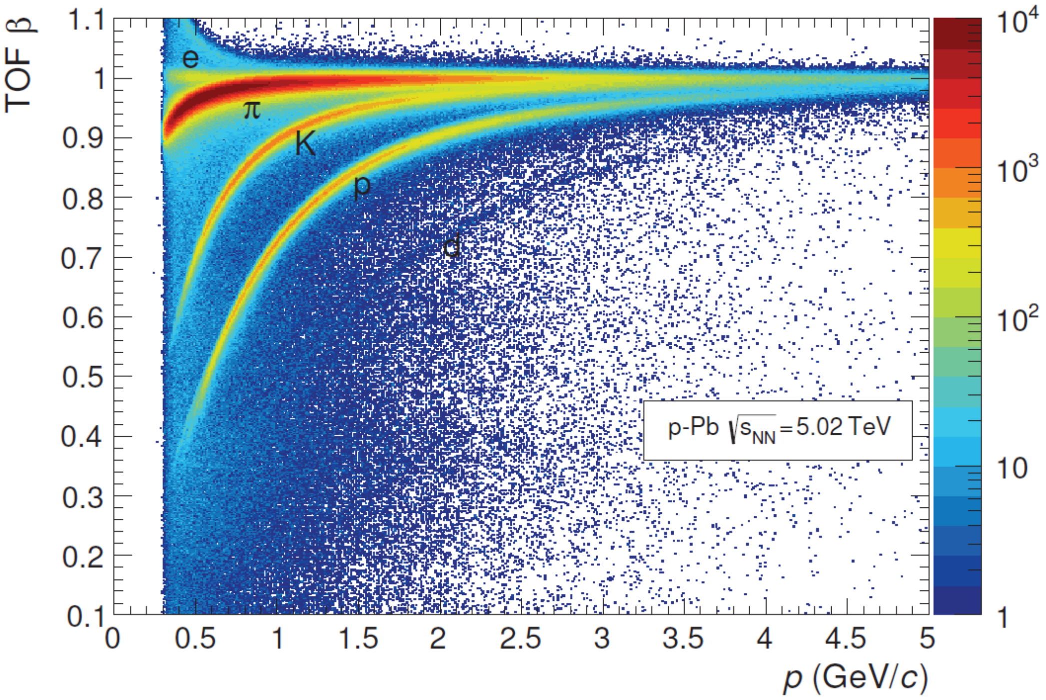

Figure 4.7. This histogram displays the energy loss versus momentum in a Pb-Pb collision at $\sqrt{s} = 2.76\,\text{TeV}$ at ALICE [29].

4.2.2 AliRoot

Finally, the measured data also has to be computed and evaluated. For that, the software framework "AliRoot" was developed [30]. It is written in C++ and has many applications as it used for the entire data analysis procedure at ALICE. It is possible to process and display data both measured by ALICE detectors and generated in statistical simulations (like Monte Carlo simulations). AliRoot is designed in such way that ALICE researchers from all over the globe are able to submit and adapt the source code for specific analysis purposes.

The basic structure of AliRoot is displayed in figure 4.8. The individual modules are described in detail in the AliRoot manual [30]. However, their functionalities will be characterized here shortly. As figure 4.8 indicates, AliRoot connects to two outer modules. The first one is called AliEn, which is needed for submitting analysis tasks to the grid, which is a worldwide computation and storage network for experiments at LHC. The second one is the ROOT framework [31]. The AliRoot code is based on ROOT, so that AliRoot uses e.g. ROOT's mathematical functions, random number generators or I/O data handling. The central component within AliRoot is the STEER module, which is used for managing runs and interfaces to the various independent detectors (like TOF, TPC, etc.). With the individual detectors, it is possible to either compute actual physical runs (AliReconstruction) or Monte Carlo simulation runs (AliSimulation) with the help of the event generator interface (EVGEN).

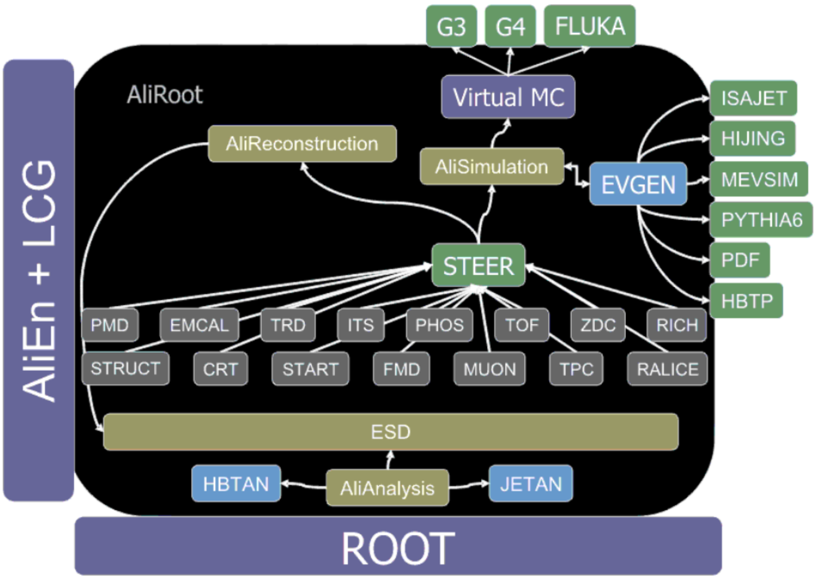

Figure 4.8. An overview of the general AliRoot architecture [32].

4.3 Invariant mass spectra

In this section, the procedure to obtain the production cross section of a certain particle, in this case the charged Ξ hyperons, will be explained. For investigating the p-Ξ^- interaction, only the Ξ^- production needs to be analyzed. However, it is a common approach to collect the data of the antiparticles to increase the statistics. This is possible as at LHC energies matter and anti-matter are produced in practically equal amounts. The cross section can be extracted differentially, e.g. depending on the transverse momentum (p_T) and pseudorapidity (η).

As a first step, the raw counts of detected Ξ candidates must be obtained, and later in the procedure, these counts will be corrected for various effects prohibiting the detection of all produced particles, e.g. the limited detector acceptance and efficiency. Since the Ξ is a non-stable particle with a mean life time of $\tau_\Xi = (1.639 \pm 0.015) \cdot 10^{-10}\,\mathrm{s}$ [33], it is not able to reach the detectors. Instead, in 99.9% of the times, it decays into a Λ and a pion:

$$\Xi^- \rightarrow \Lambda^0 + \pi^-$$

The same decay channels exist for the Ξ^+ as well, but with the respective antiparticles. Furthermore, the Λ^0 has a mean life time of $\tau_\Lambda = (2.632 \pm 0.020) \cdot 10^{-10}\,\mathrm{s}$ [34]. It decays in about 64% of the times into proton and pion:

$$\Lambda^0 \rightarrow p + \pi^-$$

Other decay channels exist as well, but are difficult to detect or the branching ratio is extremely low.

The reconstruction of the daughter particles (protons and pions) resulting from the decay of a Ξ is done by analyzing the measured experimental data event by event, identifying the primary vertex corresponding to the collision point, and the secondary vertices corresponding to the decays of longer lived particles. The measured charged particles are assigned to a particular vertex and consequently, by investigating the topology and kinematics of the observed vertices, one obtains the so called cascade candidates. These are candidates for particles whose measured decay products are 3 in total, one coming directly from the primary vertex and 2 stemming from a secondary (decay) vertex. By assigning a hypothesis about the particle types of the daughters, one could reconstruct the Ξ candidates. As the momentum $\vec{p}$ of all daughter tracks is measured, the four-momentum vector P of each daughter can be obtained using the rest mass m_0:

$$P = \begin{pmatrix} E \\ \vec{p} \end{pmatrix} \tag{4.3}$$

The energy is given by:

$$E^2 = \vec{p}^2 + m_0^2 \tag{4.4}$$

To reconstruct the Ξ candidates, the invariant mass (IM) method is applied. The IM of a specific particle is Lorentz invariant and for particles it always corresponds to the rest mass. With the given four-momentum vectors of the n daughter particles, the IM can be calculated:

$$IM = \sqrt{\left(\sum_{i=1}^{n} P_i\right)^2} \tag{4.5}$$

The decays of the Λ and the Ξ are both two-body decays. In these cases, equation 4.5 turns into:

$$IM = \sqrt{m_1^2 + m_2^2 + 2(E_1E_2 - |\vec{p_1}||\vec{p_2}| \cdot \cos(\theta))}, \tag{4.6}$$

in which θ is the angle between $\vec{p_1}$ and $\vec{p_2}$.

Due to the fact that there is always a certain detector inaccuracy, the track reconstruction and particle identification cannot be performed with perfect precision. As a result, firstly a lot of background exists, and secondly the Ξ candidates are distributed as a peak around the rest mass of $m_{\Xi^-} = 1321.71 \pm 0.07\,\mathrm{MeV}$ [33]. The AliRoot framework contains predefined classes with minimal track selection criteria which provide information on the cascade candidates. The resulting raw IM spectrum in pp collisions at 13 TeV, without the inclusion of any further selection criteria (for short this will be referred to as "without cuts" further in the text), can be seen in figure 4.9. The peak around m_Ξ is clearly visible, but a lot can be done to improve the quality of the spectrum.

To filter out the actual Ξ candidates and decrease the background, track selection cuts for both mother and daughter particles have been applied. The list of cuts, that can be seen in the appendix in table A.1, is quite extensive, which is why only some of the most common ones are discussed here to demonstrate the approach:

- DCA (*Distance of Closest Approach*) cuts: Closest distance between a track and another track or a vertex. For instance, that can be applied to the daughter tracks of the Ξ or the Λ.
- CPA (*Cosine Pointing Angle*) cuts: Cosine of the angle between a track and the primary-to-secondary vertex line. This can also be applied to decaying particles like the Ξ.
- p_T and η cuts: These cuts are made in any analysis in order not to have any harmful acceptance or efficiency effects of the detector. These effects will be discussed in the next section.

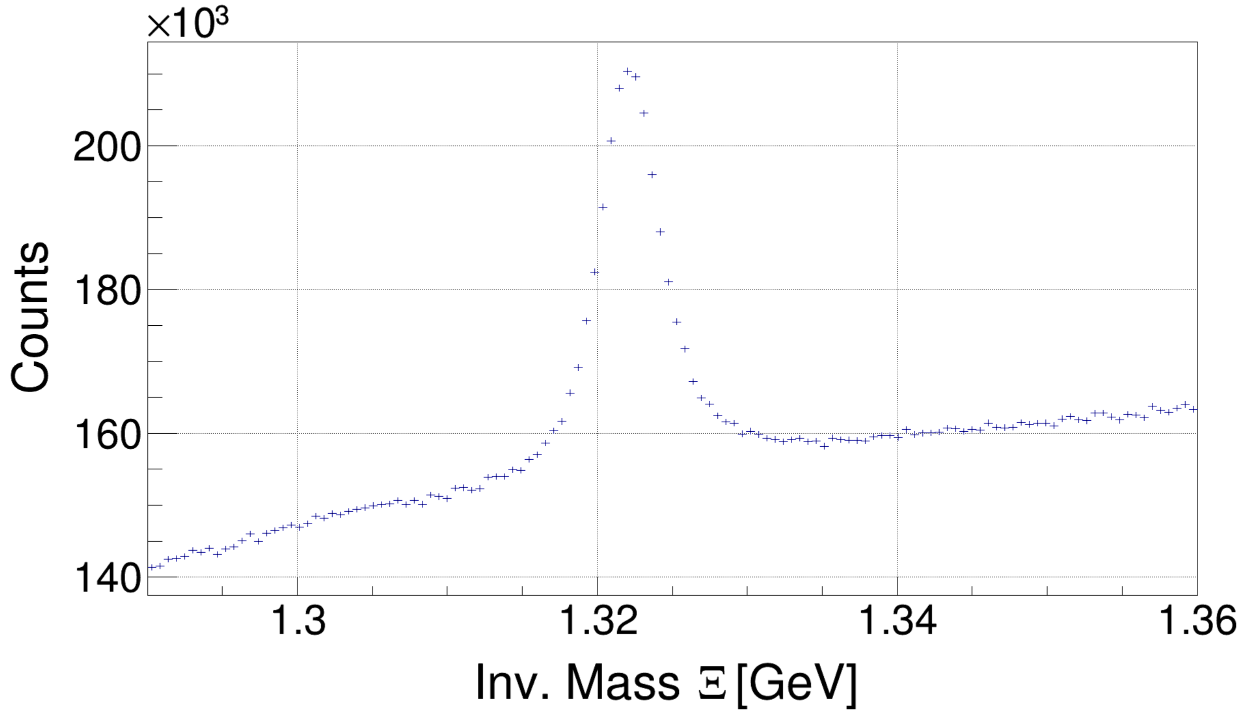

Figure 4.9. The IM spectrum without cuts from data sets Run 2.

The values of these cuts were chosen to be compatible with the ongoing Runs 2 analysis of the baryon-baryon correlation in ALICE. Applying these cuts to the IM spectrum in figure 4.9 results in a new, enhanced spectrum displayed in figure 4.10. In this spectrum, a thin peak around the rest mass of the Ξ can be seen, as much less background is present. In order to estimate the actual number of Ξ particles, a double-Gaussian distribution around the Ξ rest mass is assumed. The rather flat background can be estimated with any function that seems sensible, here a polynomial of third order is chosen. The strategy is to get the counts only of the Ξ particles, also called *signal* S, which corresponds to the integral of the double-Gaussian function. The integral of the total function (double-Gauss + polynomial) corresponds to the BS (*background-signal*), while the integral of the polynomial function only corresponds to the pure background. The fit to the data is performed with the BS-function. The free parameters of each Gaussian are the mean (common for both), the width and the normalization factor. Two Gaussians have been chosen, as they fit better to the data than one single Gaussian. The free parameters of the background polynomial are simply the four coefficients of a cubic function. By fitting this BS-function to the data using ROOT [21], the free parameters will determined. The result from that procedure is the red graph in figure 4.10.

The signal function consists only of the two Gaussians, the parameters of which can be extracted from the total BS-fit. The blue curve in figure 4.10 represents the signal only. In order to obtain the total signal this function is integrated from $-\infty$ to $+\infty$. An important side-note is that in order to fit the signal, the histogram has to be re-scaled according to the bin width, in order to obtain the proper units of counts/GeV. Hence the integration along the x-axis, which has the units of GeV, returns the number of counts or signal within the integral.

The Ξ production will be investigated depending on two observables that have already been mentioned, namely the transverse momentum p_T and the pseudorapidity η. p_T lies in the plane per-

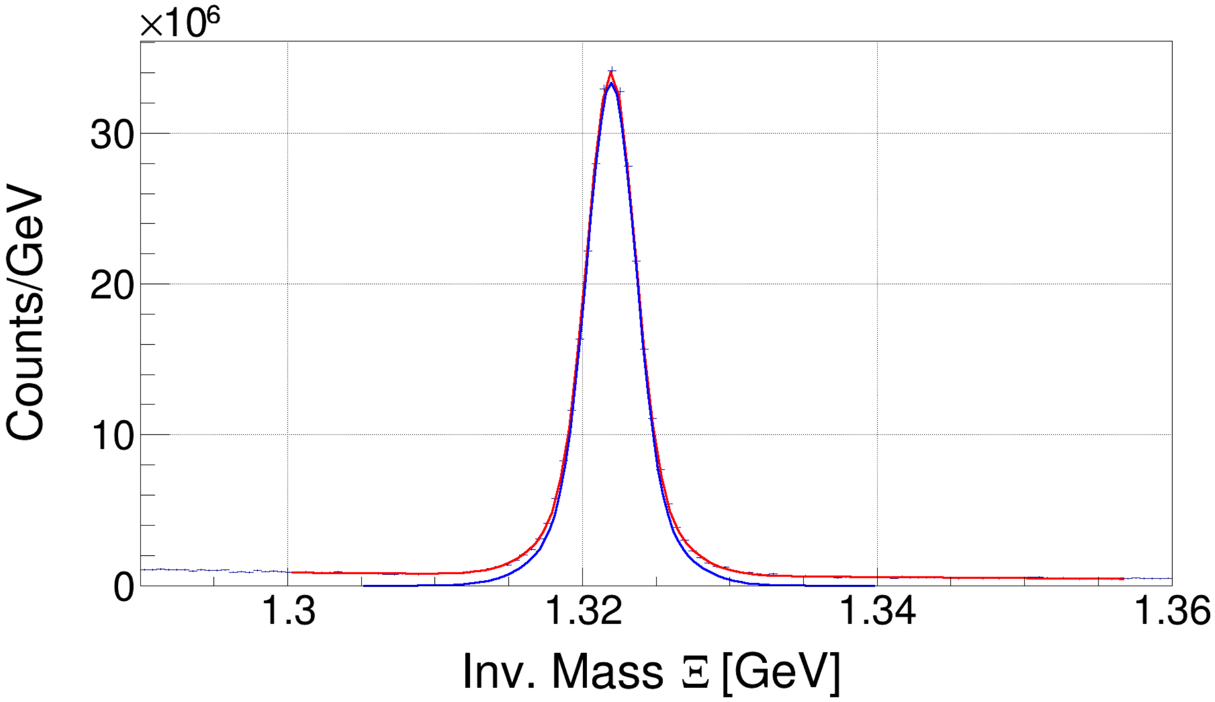

Figure 4.10. The IM spectrum with cuts from the same data sets from Run 2. The red fit represents background + signal, the blue fit only signal.

pendicular to the beam axis (z-axis):

$$p_T = \sqrt{p_x^2 + p_y^2} \tag{4.7}$$

The pseudorapidity is a spatial coordinate and depends on the polar angle θ between the beam and the particle track:

$$\eta = -\ln\left(\tan\left(\frac{\theta}{2}\right)\right) \tag{4.8}$$

The limiting values for the pseudorapidity are $\eta\left(\theta = 0^o\right) = \infty$ (parallel tracks) and $\eta\left(\theta = 90^o\right) = 0$ (perpendicular tracks). The analysis as a function of p_T is often very important, as the beam carries momentum only in the p_z direction, hence the physics related to the collision is mostly reflected in the p_T distribution of the emitted particles. The η dependence relates to the angular dependence in the acceptance limited region of the detector, hence also chosen in this analysis.

In the following, the data from LHC Run 2 in 2016 will be used. The data sets LHC16d, e, g, h, i, j, l, o and p were merged for this analysis. A three-dimensional histogram is generated after merging these data sets, containing information about p_T, η, and the IM of each particle. This happens within certain ranges that are mainly dictated by the detectors acceptance and efficiency, in this case $< p_T < 4\,GeV$, $-0.8 < \eta < 0.8$ and $1.29\,GeV$ <IM< $1.36\,GeV$. The latter cut is of course motivated by the fact that the IM window of interest should sit around the nominal mass of the Ξ. The 3d histogram can be further used to project certain dependence (p_T or η) onto the IM-axis, creating several 1d IM spectra within a flexible number of p_T- and η-bins. In each of these IM-spectra, the signal will extracted by performing a fit as described above. The integrated signal from each p_T-η bin is than used to generate a 2d histogram, which contains the signal as a function of η-vs-p_T. These spectra can be seen in figure 4.11, when track selection cuts are present. The spectra without track selection cuts can be seen in figure 4.12. Both of these spectra are still uncorrected, as the limited ability of the detector to detect each Ξ has yet to be taken into account. Both spectra have the same shape where the peak of the Ξ production lies within the p_T region $[1.0, 1.5]$ GeV and within the η region $[-0.4, 0.4]$. From there, the signal declines in every η and p_T direction. The signal for $p_T < 0.5$ GeV has not been plotted either because of the lack of statistics (with cuts), or because of too much background (without cuts). With these two spectra, it is possible to analyze the cuts themselves by comparing their signals. It becomes clear that a large amount of Ξ candidates (more than 60%) are lost due to the cuts. For the sake of having more statistics to process, generating the corrected spectra will be demonstrated without the cuts. It is also worth mentioning, that for the future femtoscopy analysis one should consider making softer cuts, because the correlation function benefits hugely from increased statistics, while any background is easily taken into account by the corrections introduced in [9], as long as the background pairs are not correlated.

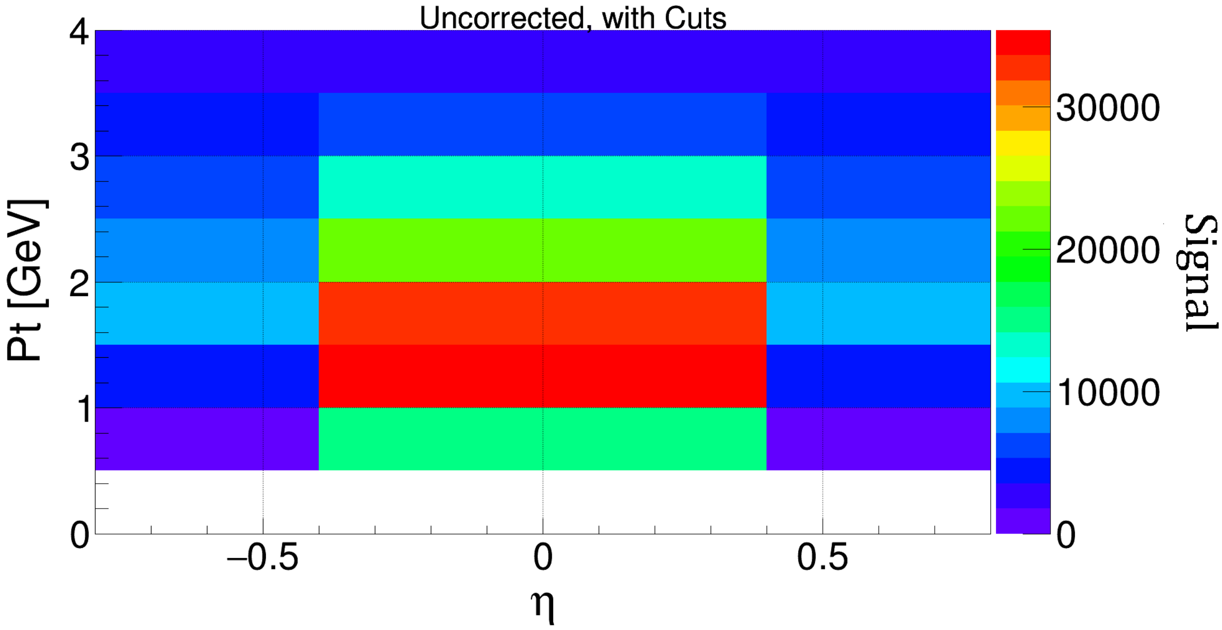

Figure 4.11. The uncorrected spectra of the detected Ξ candidates with event and track selection cuts displayed in a two-dimensional histogram with 8 p_T-bins × 4 η-bins.

4.4 Acceptance and efficiency corrections

The uncorrected spectra in figures 4.11 and 4.12 are calculated from the detected Ξ candidates, meaning that detector effects limit the Ξ yield drastically. Therefore, acceptance and efficiency corrections have to be applied. The acceptance of a detector is defined by its spatial, kinematic, etc. coverage. For instance, the ALICE detectors used for the event and track reconstruction cover a pseudorapidity of approximately $|\eta| < 0.9$, which corresponds to polar angles $45^o < \theta < 135^o$. Particles travelling outside of this angle region cannot be detected. The same is valid for p_T limitations as mentioned above, resulting in a particle-specific acceptance phase-space. On top of that, the particle detection happens only with a certain probability, even if the particle lies within the acceptance. This detection efficiency is a measure of the fraction between the reconstructed particles and the total number of produced particles. The efficiency varies depending on the position of the particle in the phase-space.

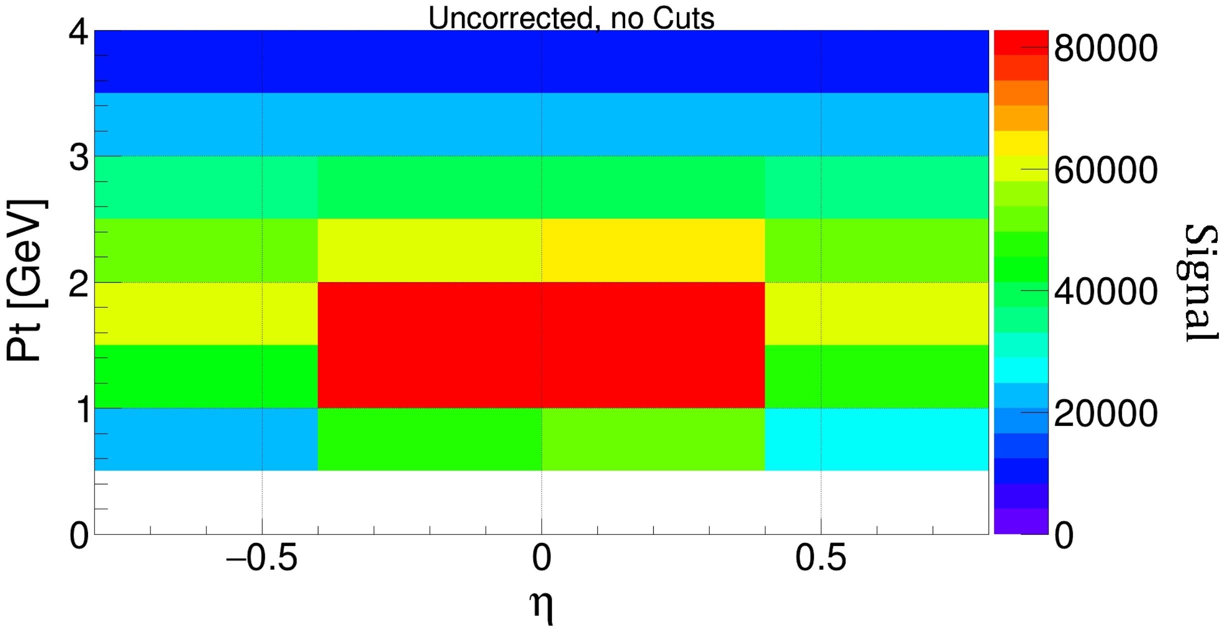

Figure 4.12. The uncorrected spectra of the detected Ξ candidates without track selection cuts displayed in a two-dimensional histogram with 8 p_T-bins $\times$ 4 η-bins.

The efficiency effects are quantified by an AEM (*Acceptance and Efficiency Matrix*), which gives the efficiency as a function of some variables, in this analysis p_T and η. Hence the total yield of particles can be obtained by multiplying the AEM to the uncorrected data. The AEM is obtained with the help of Monte-Carlo (MC) simulations, by simulating first the collision process and populating the available 4π (full) phase-space. These are called true-MC samples and in ALICE they have been generated by using PYTHIA 8 ([35]). The next step is to simulate all detector related effects (full-scale simulation) by running the PYTHIA output through the Geant framework ([36]), which in ALICE is also performed centrally for all true-MC samples. To correct the experimental yield $\mathcal{S}_{exp,i,j}$ (in p_T-bin i and η-bin j) and obtain the total yield $\mathcal{S}_{tot,i,j}$ one can use the output of the Monte-Carlo in the form:

$$\mathcal{S}_{source,i,j} = \mathcal{S}_{exp,i,j} \cdot \frac{\mathcal{S}_{trueMC,i,j}}{\mathcal{S}_{fullMC,i,j}}, \tag{4.9}$$

where $\mathcal{S}_{fullMC}$ and $\mathcal{S}_{trueMC}$ correspond to the number of Ξ particles in the full-scale and true MC samples. The full-scale simulation includes not only the detector effects, but the reconstruction of the particles is performed identically to the real experimental data, including the cascade reconstruction and subsequent topological cuts. In fact, to make sure that the full-scale MC samples are as realistic as possible, the central ALICE MC production is performed by creating different simulations for each data set, where the MC data contains all detector conditions as they occurred run by run. The MC data sets used in this analysis are LHC17f6, f9, d17, f5, d3, e5, a2, d16 and d18 from Run 2.

In figure 4.13, the result of the true MC simulation can be seen. It displays the Ξ production directly from the source without any event or track selection cuts. The particles in true MC simulations are generated with an ID according to the Monte Carlo particle numbering scheme ([37]), meaning that Ξs can simply be counted without any background. As the true MC simulations populate the entire phase-space without any gaps in the acceptance, the entries are homogeneously distributed even in the lowest p_T-bins. Also, figure 4.13 shows that the peak of these spectra is shifted to transverse momenta below 1 GeV. The distribution of the yield as a function of p_T usually follows approximately a Boltzmann distribution. The η-distribution is far more widespread, being symmetric around 0. In figure 4.14, the full scale simulation including detector effects can be seen. This is supposed to replicate the experimental yield, hence the same event and track selection cuts have to made as in the experiment. Here, no track selection cuts are assumed. In some of the bins too much background exists and prevents obtaining stable fits, which is why only bins with a purity of at least 10 % are included. Nonetheless, the full MC spectra have the same approximate shape as the experimental data in figure 4.12. Especially their p_T- and η-peaks are in the same regions, demonstrating that the MC simulation represents the detector accurately, and the initial kinematics distributions are realistic. After generating these two spectra, the AEM can be calculated by dividing these two distributions bin-by-bin. This matrix can then be used to correct the experimental yield, the result of which is shown in figure 4.15.

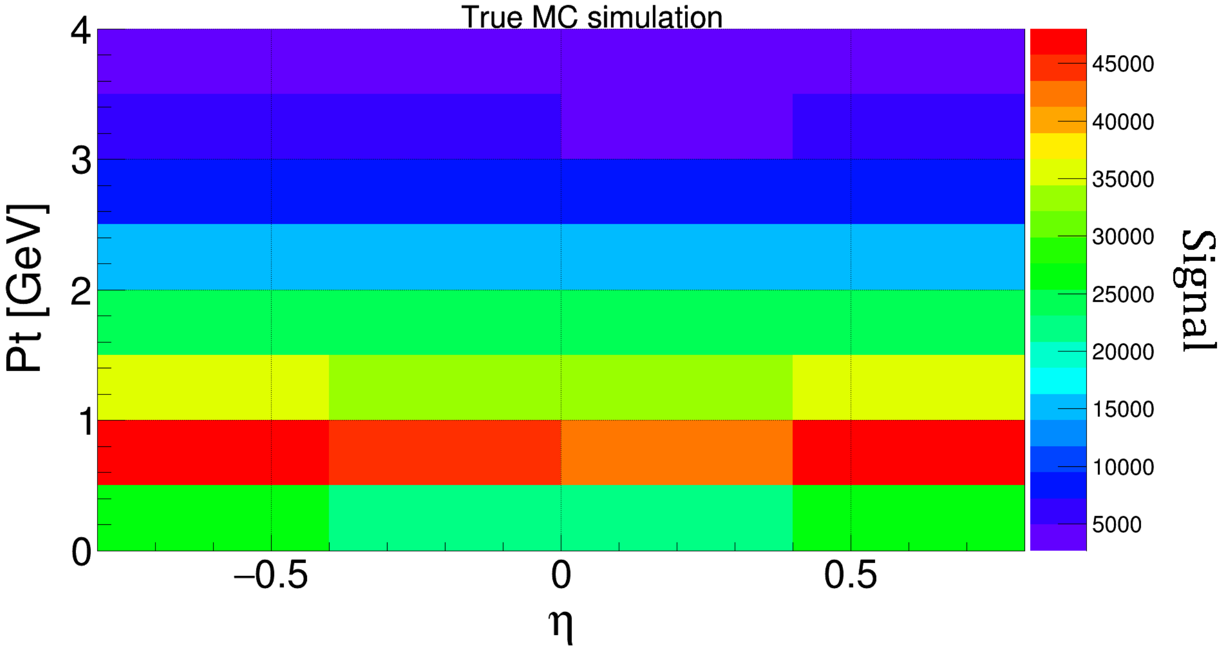

Figure 4.13. The true MC simulation anchored to the experimental data sets used above. This simulation includes only the Ξ production in all events via an event generator.

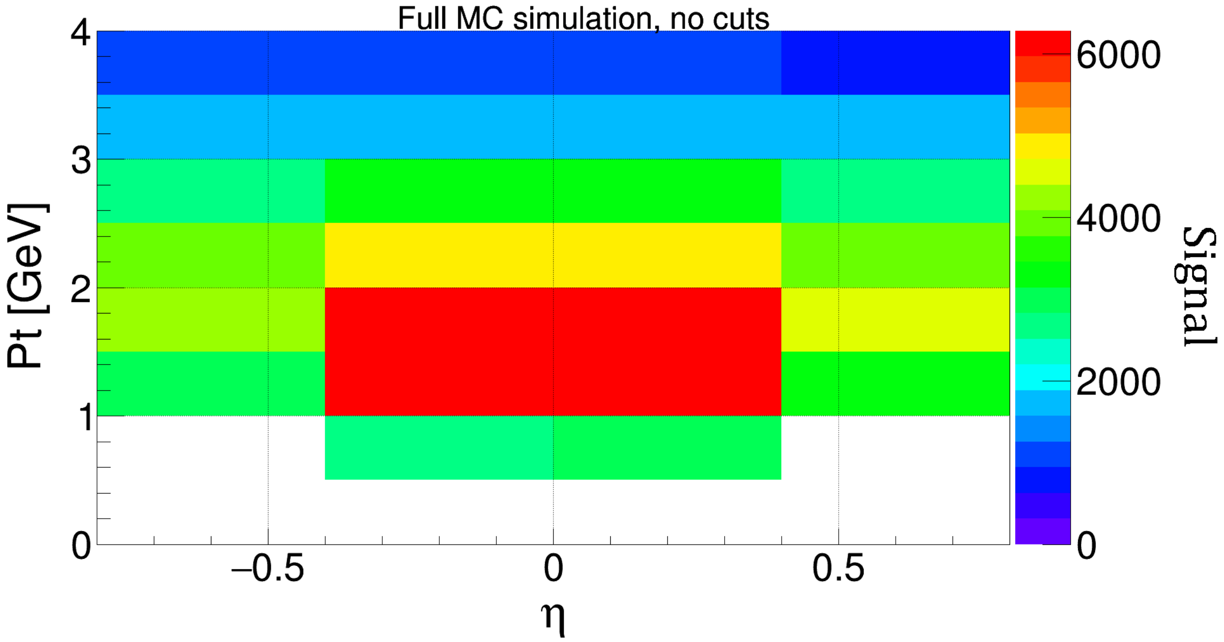

Figure 4.14. The full MC simulation of the Ξ production without track selection cuts. This simulation also includes the influence of the detector.

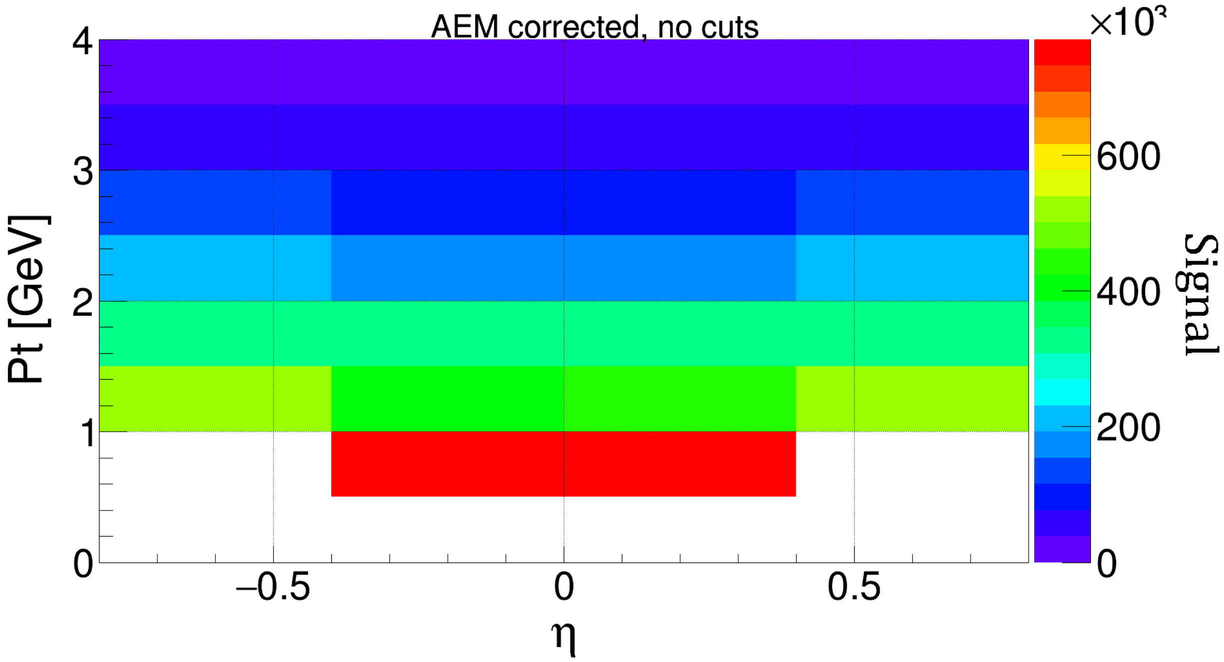

Figure 4.15. The Ξ production spectra including acceptance and efficiency corrections obtained from MC simulations.

4.5 Further corrections

With the help of the Monte Carlo simulations, a major correction has already been made. In order to get the cross section a few more steps are necessary. The first one is the branching ratio correction due to the fact that not every Λ can be detected, as there is a second major decay channel that involves a neutron and a neutral pion:

$$\Lambda^0 \rightarrow n + \pi^0 \tag{4.10}$$

The probability of this decay is 34%. Consequently, the final result has to include a constant factor that considers the probability of the Λ decaying into a proton and a pion, which is $\varepsilon^{branch} = 63.9 \pm 0.5$ ([34]). Another correction is the trigger efficiency related to the probability not to trigger on a pp collision that contains a Ξ. A related analysis in the ongoing di-lepton analysis in our group revealed that this factor is consistent with 1 and can be neglected ($\varepsilon^{trig} = 1$). A similar correction is related to the probability of not reconstructing the primary vertex for an event containing a Ξ. This probability is also negligible ($\varepsilon^{vtx} = 1$). All cited final results, as well as the corrected spectrum in figure 4.16, are corrected for these effects.

The binning used so far consists of 8 × 4 bins in p_T and η. Especially when track selection cuts are present, the binning cannot be made any finer because there is not enough statistics in the current full MC simulation to perform proper fits. However, a finer binning allows for a more differential analysis and thereby makes the correction procedure more independent of the PYTHIA event generator. All spectra presented above indicate that the η distribution is symmetrical around 0. That makes it possible to display the spectra as a function of $|\eta|$ instead of η, which will double the effective statistics in the η bins. Here, a $|\eta|$-bin width of 0.2 will be chosen, which can also be seen in the final result (figure 4.16). These spectra are still without track selection cuts. Due to too much background, some of the fits in the IM spectra were not precise enough to be included in this signal matrix. In particular, a purity of at least 10 % was demanded in the full MC simulations. The experimental data were also affected by background, particularly in the lower p_T-bins. Thus in order to include the result from a specific bin we demand that the IM fit produces $\chi^2/ndf < 4$. The conditions are applied both to the full MC and experimental data sets.

4.6 The cross section

With the help of the corrected spectra, the differential and total production cross section can be calculated. Due to the limited acceptance of the detector, some of the bins in the differential spectrum are empty. We could partially correct for that by fitting the yields, in different η bins, as a function of p_T using a Boltzmann distribution. This way the extrapolated spectra will be extended into the geometrical acceptance of ALICE within $|\eta| < 0.8$. The normalized Boltzmann distribution is given by:

$$f(p_T) = N \cdot p_T \sqrt{p_T^2 + m^2}\, \frac{\exp\left(-\frac{\sqrt{p_T^2+m^2}}{T}\right)}{T \cdot (m^2 + 2mT + 2T^2)\exp\left(-\frac{m}{T}\right)} \tag{4.11}$$

in which N and the (effective) temperature T are free parameters. N coincides with the p_T integrated Ξ yield. By performing this fit for each $|\eta|$ the production cross section can be presented in a differential form as function of pseudorapidity $|\eta|$, the total yield can be obtained by summing

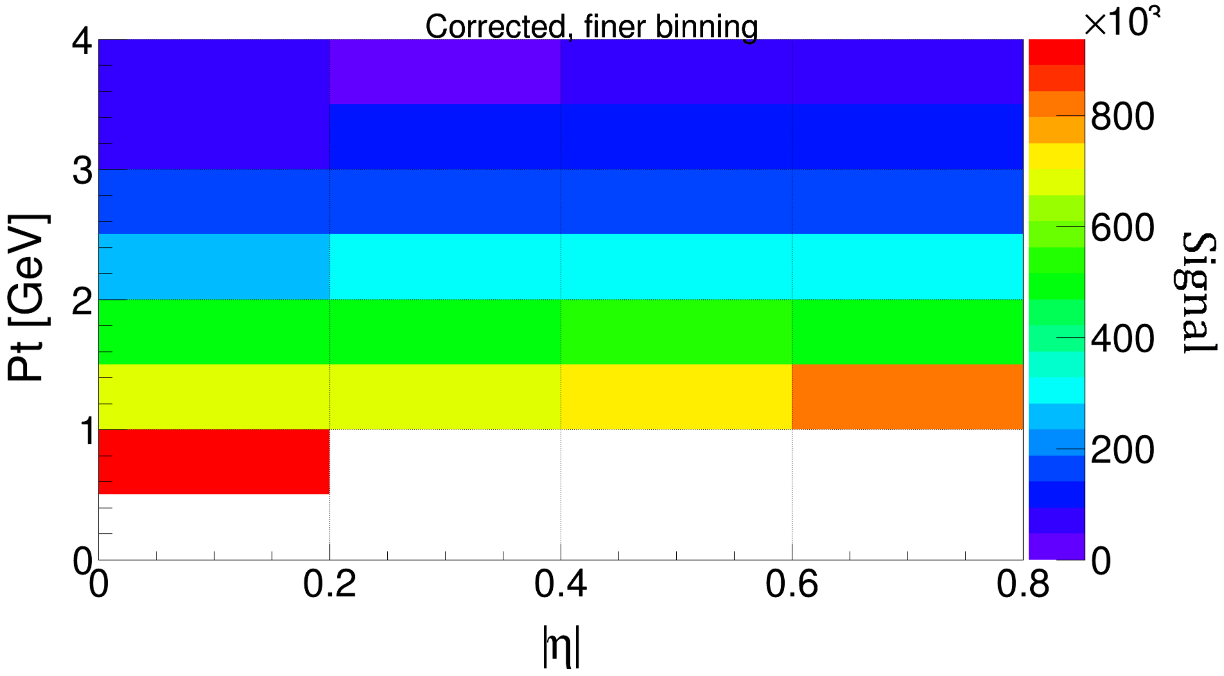

Figure 4.16. The corrected Ξ production spectra without track selection cuts after all major corrections.

the results together. An example of the Boltzmann fit for one $|\eta|$-bin ($0.2 < |\eta| < 0.4$) is shown in figure 4.17. The result for the total yield is $N^{4\times|\eta|} = 1.1\cdot 10^7 \pm 2.1\cdot 10^4$. To convert this result into a cross section on can use the relation:

$$\left.\frac{d\sigma}{d|\eta|}\right|_{|\eta|<0.8} = \frac{1}{\mathscr{L}}\frac{S}{\Delta\eta\,\varepsilon^{branch}\varepsilon^{trig}\varepsilon^{vtx}\varepsilon^{AEM}} \tag{4.12}$$

where S is the measured signal (yield), corrected for all of the effects previously discussed, and normalized with the luminosity $\mathscr{L}$, which is related to the number of analyzed minimum bias pp events (with V0AND trigger condition) and the corresponding cross section $\sigma_{pp}^{V0AND} = (57.8 \pm 2.9)\,mb$ [38]:

$$\mathscr{L} = \frac{N^{V0AND}}{\sigma_{pp}^{V0AND}} \tag{4.13}$$

where N^{V0AND} is defined as the number of events considered for the analysis $N_{evt} = 2.4\times 10^8$ corrected with the respective vertex reconstruction efficiency $\varepsilon_{evt}^{vtx} = 0.973 \pm 0.001$:

$$N^{V0AND} = \frac{N_{evt}}{\varepsilon_{evt}^{vtx}}. \tag{4.14}$$

ε_{evt}^{vtx} is the probability to have an event satisfying the trigger condition, without triggering.

The result for the differential cross section without track selection cuts is:

$$\left.\frac{d\sigma}{d|\eta|}\right|_{|\eta|<0.8}^{no\,Cuts} = (3.31 \pm 0.17)\,mb$$

The same procedure has been done when track selection cuts were present, yielding:

$$\left.\frac{d\sigma}{d|\eta|}\right|_{|\eta|<0.8}^{with\,Cuts} = (3.8 \pm 0.19)\,mb$$

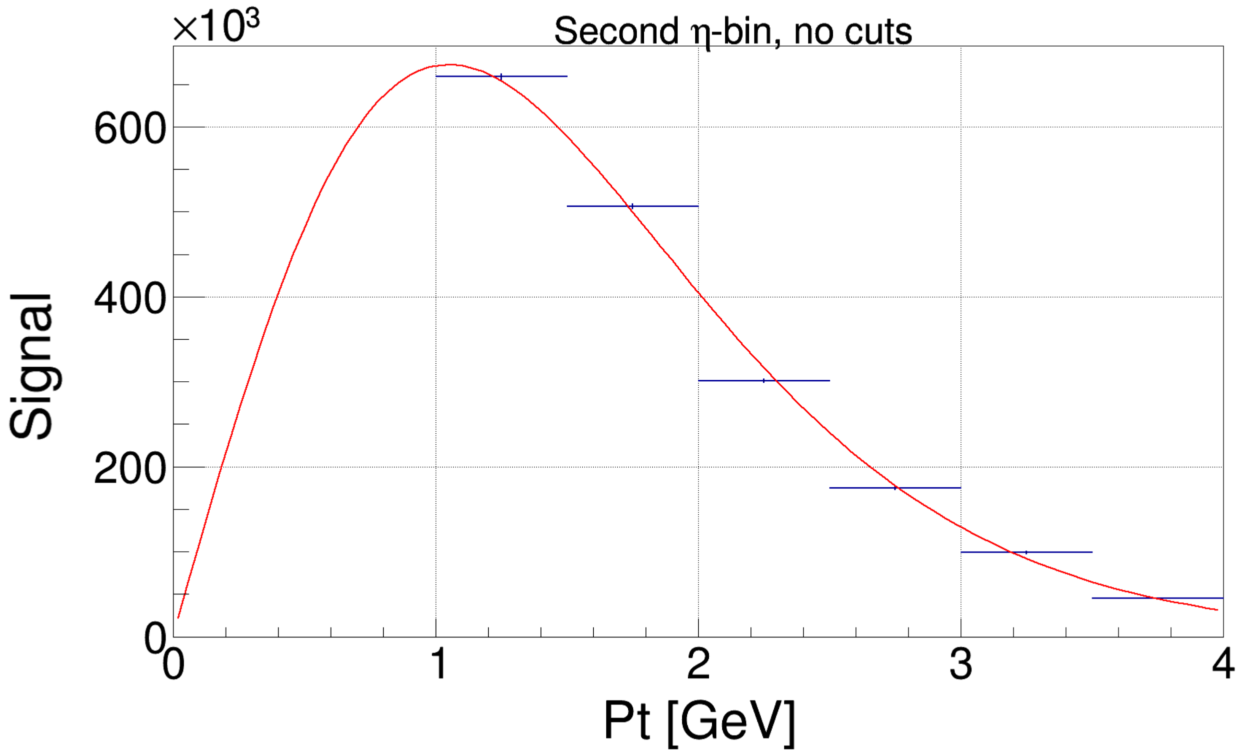

Figure 4.17. The p_T distribution along the second $|\eta|$-bin ($0.2 < |\eta| < 0.4$) of the corrected spectra without track selection cuts, fitted with a Boltzmann function.

The Ξ production is independent of any cuts, hence the results should be equal. The fact that they are not points to potential systematic biases in the analysis procedure. As this is only a first look into the Ξ production, this result makes no claim be highly precise, as there are multiple steps that can be further optimized. A trivial optimization would be a better constrain on the starting values and limits of the fit parameters, which might improve the quality of the fitting procedure and allow to extract the yield in some of the bins with lower purity. The full Run 2 data sample contains more than 1 billion events, while this analysis uses only c.a. 20% of the available statistics, hence another trivial improvement can be done by analyzing the full statistics, which will allow to make the differential analysis with finer binning, given enough statistics in the Monte-Carlo data, which is currently not available. Finally it should be stressed that the modeling of the background can be done using more sophisticated methods, e.g. by performing a side-band analysis as described here [39]. This will result in a much more accurate determination of the signal compared to the current analysis. At the moment the signal and background are fitted together, which might introduce an artificial correlation between the two, resulting in a large systematic uncertainty.

In this analysis we do not perform an extensive investigation of the systematic uncertainty, nevertheless as a rough estimation we can use the deviation between the two obtained results.

$$\left.\frac{d\sigma}{d|\eta|}\right|_{|\eta|<0.8} = (3.56 \pm (0.18)^{stat} \pm (0.25)^{syst})\,mb$$

is the mean value of the results quoted above.

To cross check these values, another method can be tried out, too. To obtain the total yield and calculate the cross section, the binning of the histogram can be changed to one $|\eta|$-bin and 32 p_T-bins, creating a single p_T distribution. In figure 4.18, this distribution without track selection cuts can be seen. Again, bins below 1 GeV have been neglected because of too much background that disturbs a precise fitting procedure. This effect is still noticeable in the first two p_T-bins above 1 GeV. After normalizing the data to the new p_T-bin width of 0.125 GeV, the total yield including statistical error can be obtained from the fit: $N^{1\times|\eta|} = 1.4 \cdot 10^7 \pm 2.3 \cdot 10^5$. With the new signal and AEM calculation, and also new bin width of $\Delta|\eta| = 0.8$, the differential cross sections can be calculated. This has also been done with and without track selection cuts:

$$\frac{d\sigma^{1\times 32}}{d|\eta|}\Bigg|_{|\eta|<0.8}^{no\,Cuts} = (3.95 \pm 0.2)\,mb$$

$$\frac{d\sigma^{1\times 32}}{d|\eta|}\Bigg|_{|\eta|<0.8}^{with\,Cuts} = (4.67 \pm 0.23)\,mb$$

These results are probably less accurate, as they imploy only a single differential analysis and any η dependence is not included. Also the instability of the fit in the first few p_T bins may lead to larger systematic uncertainties. Nevertheless the results are comparable to the result obtained from the double-differential analysis.

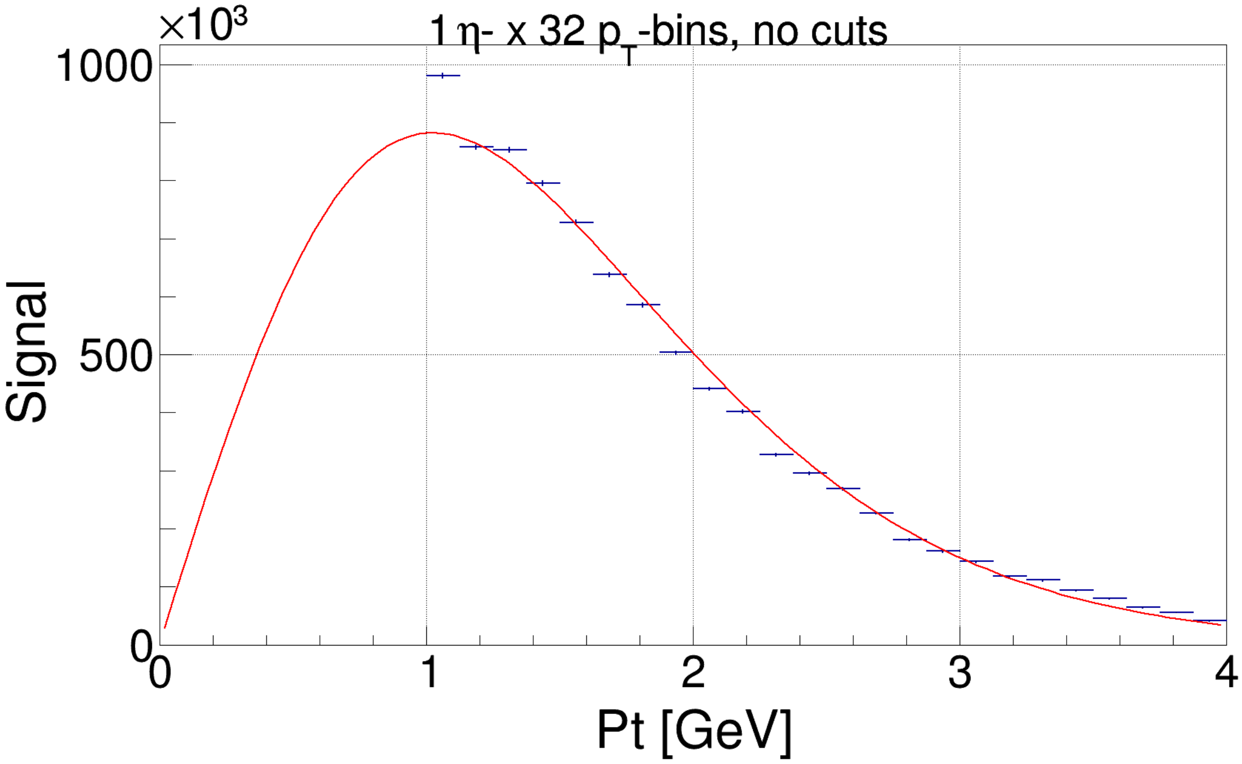

Figure 4.18. The p_T distribution over all $|\eta|$-bins without track selection cuts fitted with a Boltzmann function.

Finally, assuming the Ξ production in each η-bin follows its own Boltzmann distribution, as in figure 4.17, one can extrapolate the corrected spectra and fill up each bin with the total yield obtained by integrating the fit function in the range of the corresponding p_T-bin. The result of these extrapolated spectra, without cuts, can be seen in figure 4.19. The maximum value of all those fits sits at around 1 GeV. This is expected and compatible to previous ALICE results from pp collisions at 7 TeV [40].

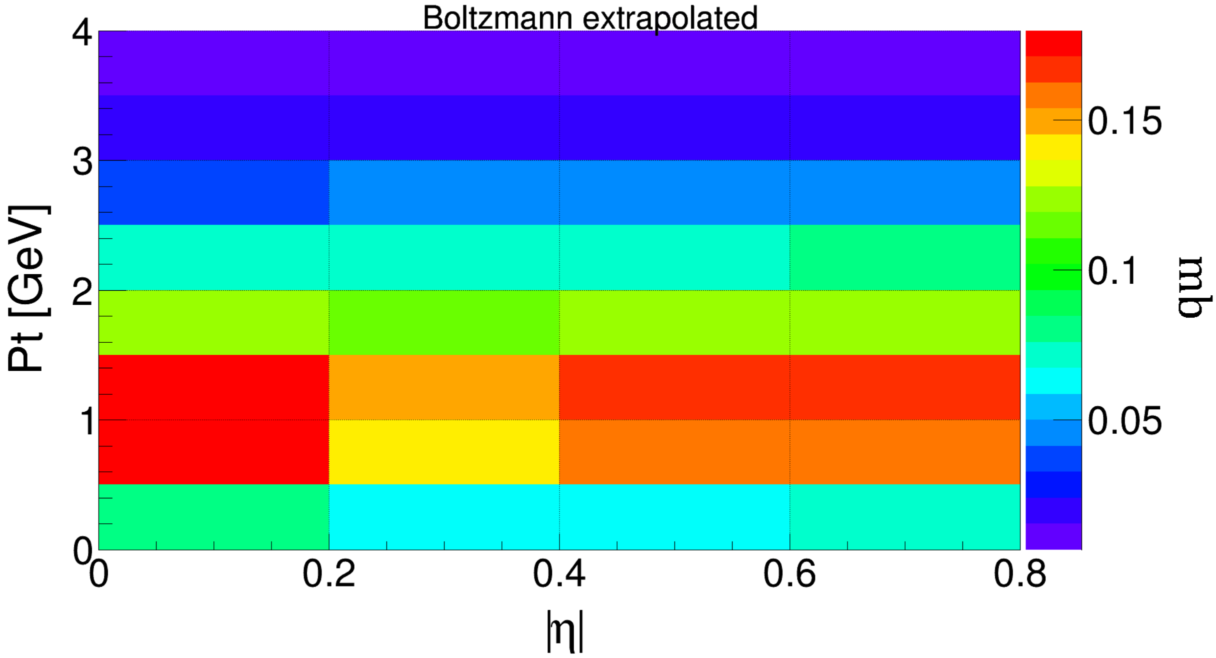

Figure 4.19. The spectra extrapolated with the Boltzmann fit.

5 Summary and outlook

This thesis concentrates on two-body N-Y interactions, as they play an important role in the determination of the equation of state, which relates to the description of neutron stars. These interactions can be investigated with the help of the method of femptoscopy, which is an alternative to traditional scattering experiments, and is best suited for analyzing interactions when the two particles have low relative momenta. In femtoscopy, the theoretical definition of the correlation function $C_{theo}(k^*)$ includes the potential of interest and an emitting source. In an experiment the measured correlation function contains impurities and residual correlations, which can be modeled and included in the fit function $C_{fit}(k^*)$.

In chapter 3, the p-Λ was investigated. The motivation is the observed dip in the correlation function at $k^* > 100$ MeV, which in previous analyses is attributed to non-femtoscopic correlations. Here we investigate the possibility, that the observed effect is related to the repulsive core of the p-Λ interaction. To model it the Usmani potential is used, which contains a phenomenological repulsive core, the parameters of which can be modified and translated to a correlation function. As the Usmani potential is fitted to existing scattering data, our goal was to find a variation of the repulsive core, introduce a slight depletion in the correlation function above $k^* > 100$ MeV, but preserve the scattering parameters. However those investigations revealed that $C(k^*)$ is mostly sensitive to the scattering parameters, and rather insensitive to modifications of the shape of the repulsive core. Further the experimental data were fitted by allowing maximum freedom of the fit parameters, ignoring the constraints imposed by the scattering data. Even in this case the observed structure at $k^* > 100$ MeV cannot be reproduced, highlighting that this is indeed not an effect of the potential. A solution to this problem is already shown in [9], where this structure is modeled by a linear baseline, which is associated with to non-femtoscopic contributions. However the exact origin of these correlations are still unknown. Future investigations should verify if this effect can be attributed to the other ingredient in the correlation function, namely the emission source, which is currently assumed to be static, isotropic Gaussian source with a certain width (see equation 2.5), which might be an oversimplification. A non-Gaussian source can result in a different profile of $C(k^*)$, and in fact some transport models like EPOS [41] do predict non-Gaussianity in the emission. Further, effects of short-lived resonances not included in the residual correlations might change the profile of the source, while collective effects, which are now known to exist even in pp collisions [42], can introduce certain asymmetries to the source. All these effects can result introduce a non-static (time-dependent) source. It is far beyond the scope of the current work to investigate these effects, but they should be considered in future analyzes.

In chapter 4, the importance of the p-Ξ^- interaction for neutron stars was discussed. In particular one could test lattice potentials to verify their overall validity in the N-Ξ sector. The latest lattice results from the HAL-QCD collaboration predict a repulsive n-Ξ^- interaction, which will stiffen the equation of state and might be a step towards solving the hyperon puzzle related to the existence of massive neutron stars. In the current work we make the first step towards investigating Ξ^- particles in ALICE, by investigating the pp collision system at 13 TeV, measuring and correcting the Ξ yield for acceptance and efficiency. The total measured cross section withing the geometrical acceptance is $(3.56 \pm (0.18)^{stat} \pm (0.25)^{syst})\, mb$. Further we have seen that the cuts currently used for the Ξ reconstruction in femtoscopic analysis cut out more that 60 % signal, which demands for a further investigation and fine-tuning of these cuts, before they are applied to a femtoscopic analysis. This will be needed in order to decrease the statistical uncertainty on the correlation function.

A Appendix

Selection criterion	Value
Daughter track selection criteria	
Pseudorapidity	$\|\eta\| < 0.8$
TPC cluster	$n_{\mathrm{TPC}} > 70$
Transverse Momentum	$p_{\mathrm{T}} > 0.3\,\mathrm{GeV}/c$
Distance of closest approach	$\mathrm{DCA}_{\mathrm{Bachelor}} > 0.05\,\mathrm{cm}$
Distance of closest approach	$\mathrm{DCA}_{\mathrm{v0Daughters}} > 0.04\,\mathrm{cm}$
Particle identification	$\|n_{\sigma,\mathrm{TPC}}\| < 4$
Λ *selection criteria*	
Λ Pointing angle α	$\cos\alpha > 0.97$
Transverse radius of the Λ decay vertex r_{xy}	$1.4 < r_{xy} < 200\,\mathrm{cm}$
DCA of the daughter tracks at the Λ decay vertex	$\mathrm{DCA}(\|p,\pi\|) < 1.6\,\mathrm{cm}$
DCA of the Λ to the PV	$\mathrm{DCA} > 0.07\,\mathrm{cm}$
Λ selection	$\|\mathrm{M}_{\mathrm{p}\pi} - \mathrm{M}_{\Lambda,\mathrm{PDG}}\| < 6\,\mathrm{MeV}/c^2$
Ξ *selection criteria*	
Ξ p_T range	$0.01 < p_T < 4.05\,\mathrm{GeV}$
Ξ Pointing angle α	$\cos\alpha > 0.97$
Transverse radius of the Ξ decay vertex r_{xy}	$0.8 < r_{xy} < 200\,\mathrm{cm}$
DCA of the daughter tracks at the Ξ decay vertex	$\mathrm{DCA}(\|p,\pi,\pi\|) < 1.6\,\mathrm{cm}$
Ω rejection	$1.667 < \mathrm{M}_{pK\pi^-} < 1.677\,\mathrm{GeV}/c^2$

Table A.1. Ξ selection criteria.

Bibliography

[1] J. Antoniadis *et al.*, “A Massive Pulsar in a Compact Relativistic Binary”, *Science*, vol. 340, 2013.

[2] P. Demorest, T. Pennucci, S. Ransom, M. Roberts, and J. Hessels, “Shapiro Delay Measurement of A Two Solar Mass Neutron Star”, *Nature*, vol. 467, pp. 1081–1083, 2010.

[3] R. Tolman, “Static solutions of Einstein’s field equations for spheres of fluid”, *Physical Review*, vol. 55, pp. 364–373, 1939.

[4] J. R. Oppenheimer and G. M. Volkoff, “On Massive Neutron Cores”, *Physical Review*, vol. 55, pp. 374–381, 1939.

[5] F. Özel and P. Freire, “Masses, radii, and the equation of state of neutron stars”, *Annual Review of Astronomy and Astrophysics*, vol. 54, pp. 401–440, 2016.

[6] I. Bombaci, “The Hyperon Puzzle in Neutron Stars”, *JPS Conf. Proc.*, vol. 17, 2017.

[7] D. Lonardoni, A. Lovato, S. Gandolfi, and F. Pederiva, “Hyperon Puzzle: Hints from Quantum Monte Carlo Calculations”, *Phys. Rev. Lett.*, vol. 114, p. 092 301, 2015.

[8] M. A. Lisa, S. Pratt, R. Soltz, and U. Wiedemann, “Femtoscopy in relativistic heavy ion collisions”, *Ann. Rev. Nucl. Part. Sci.*, vol. 55, pp. 357–402, 2005.

[9] S. Acharya *et al.*, “p-p, p-Λ and Λ-Λ correlations studied via femtoscopy in pp reactions at $\sqrt{s} = 7$ TeV”, 2018. arXiv: `1805.12455 [nucl-ex]`.

[10] S. Pratt, “Pion Interferometry for Exploding Sources”, *Phys. Rev. Lett.*, vol. 53, pp. 1219–1221, 1984.

[11] R. Lednicky, “Finite-size effects on two-particle production in continuous and discrete spectrum”, *Phys. Part. Nucl.*, vol. 40, pp. 307–352, 2009.

[12] S. Veerasamy and W. N. Polyzou, “A momentum-space Argonne V18 interaction”, *Phys. Rev.*, vol. C84, p. 034 003, 2011.

[13] O. Arnold, “Study of the hyperon-nucleon interaction via femtoscopy in elementary systems with HADES and ALICE”, *Technische Universität München*, 2017.

[14] D. Mihaylov *et al.*, “A femtoscopic Correlation Analysis Tool using the Schrödinger equation (CATS)”, *The European Physical Journal C*, 2018.

[15] F.-q. Wang and S. Pratt, “Lambda proton correlations in relativistic heavy ion collisions”, *Phys. Rev. Lett.*, vol. 83, pp. 3138–3141, 1999. DOI: `10.1103/PhysRevLett.83.3138`.

[16] R. Lednicky and V. L. Lyuboshits, “Final State Interaction Effect on Pairing Correlations Between Particles with Small Relative Momenta”, *Sov. J. Nucl. Phys.*, vol. 35, p. 770, 1982, [Yad. Fiz.35,1316(1981)].

[17] G. Alexander, U. Karshon, A. Shapira, G. Yekutieli, R. Engelmann, H. Filthuth, and W. Lughofer, “Study of the lambda-n system in low-energy lambda-p elastic scattering”, *Phys. Rev.*, vol. 173, pp. 1452–1460, 1968.

[18] B. Sechi-Zorn, B. Kehoe, J. Twitty, and R. A. Burnstein, "Low-energy lambda-proton elastic scattering", *Phys. Rev.*, vol. 175, pp. 1735–1740, 1968.

[19] J. A. Kadyk, G. Alexander, J. H. Chan, P. Gaposchkin, and G. H. Trilling, "Lambda p interactions in momentum range 300 to 1500 mev/c", *Nucl. Phys.*, vol. B27, pp. 13–22, 1971.

[20] J. J. Sakurai, *Modern quantum physics.* Cambridge: Cambridge University Press, 1995, pp. 410–418.

[21] ROOT Data Analysis Framework, *ROOT Reference Guide.* [Online]. Available: `https://root.cern.ch/doc/v608/classTH1.html` (visited on 09/06/2018).

[22] Z. Chajecki and M. Lisa, "Global Conservation Laws and Femtoscopy of Small Systems", *Phys. Rev.*, vol. C78, p. 064 903, 2008.

[23] J. Adam *et al.*, "Insight into particle production mechanisms via angular correlations of identified particles in pp collisions at $\sqrt{\mathrm{s}} = 7$ TeV", *Eur. Phys. J.*, vol. C77, no. 8, p. 569, 2017.

[24] S. Weissenborn, D. Chatterjee, and J. Schaffner-Bielich, "Hyperons and massive neutron stars: the role of hyperon potentials", *Nucl. Phys.*, vol. A881, pp. 62–77, 2012.

[25] T. Hatsuda, K. Morita, A. Ohnishi, and K. Sasaki, "$p\Xi^-$ Correlation in Relativistic Heavy Ion Collisions with Nucleon-Hyperon Interaction from Lattice QCD", *Nucl. Phys.*, vol. A967, pp. 856–859, 2017.

[26] J. Alme *et al.*, "The ALICE TPC, a large 3-dimensional tracking device with fast readout for ultra-high multiplicity events", *Nucl. Instrum. Meth.*, vol. A622, pp. 316–367, 2010.

[27] K. Aamodt *et al.*, "The ALICE experiment at the CERN LHC", *JINST*, vol. 3, 2008.

[28] K. Aamodt *et al.*, "Alignment of the ALICE Inner Tracking System with cosmic-ray tracks", *JINST*, vol. 5, P03003, 2010.

[29] Abelev *et al.*, "Performance of the alice experiment at the cern", *International Journal of Modern Physics A*, vol. 29, 2013.

[30] Alice Collaboration, *AliRoot Manual.* [Online]. Available: `http://alice-offline.web.cern.ch/AliRoot/Manual.html` (visited on 07/20/2018).

[31] R. Brun and F. Rademakers, "ROOT — An object oriented data analysis framework", *Nuclear Instruments and Methods in Physics*, 1998.

[32] Alice Collaboration, *AliRoot Manual.* [Online]. Available: `http://alice-offline.web.cern.ch/AliRoot/Manual.html#General` (visited on 07/20/2018).

[33] Particle Data Group, Ξ *baryons.* [Online]. Available: `http://pdglive.lbl.gov/Particle.action?init=0&node=S022&home=BXXX030` (visited on 09/03/2018).

[34] PDG, Λ *baryons.* [Online]. Available: `http://pdglive.lbl.gov/Particle.action?init=0&node=S018&home=BXXX020` (visited on 09/03/2018).

[35] *PYTHIA 8.2.* [Online]. Available: `http://home.thep.lu.se/Pythia/` (visited on 09/11/2018).

[36] *GEometry ANd Tracking - GEANT.* [Online]. Available: `http://www.geant4.org/geant4/` (visited on 09/03/2018).

[37] *Monte Carlo particle numbering scheme.* [Online]. Available: `http://pdg.lbl.gov/2007/reviews/montecarlorpp.pdf` (visited on 09/25/2018).

[38] "ALICE luminosity determination for pp collisions at $\sqrt{s} = 13$ TeV", Jun. 2016. [Online]. Available: `https://cds.cern.ch/record/2160174`.

[39] J. Berger-Chen, "The Production of K0 in p+p Reactions at 3.5 GeV", *Technische Universität München*, 2015.

[40] B. Abelev *et al.*, “Multi-strange baryon production in *pp* collisions at $\sqrt{s} = 7$ TeV with ALICE”, *Phys. Lett.*, vol. B712, pp. 309–318, 2012. DOI: `10.1016/j.physletb.2012.05.011`. arXiv: `1204.0282 [nucl-ex]`.

[41] T. Pierog, I. Karpenko, J. M. Katzy, E. Yatsenko, and K. Werner, “EPOS LHC: Test of collective hadronization with data measured at the CERN Large Hadron Collider”, *Phys. Rev.*, vol. C92, no. 3, p. 034 906, 2015. DOI: `10.1103/PhysRevC.92.034906`. arXiv: `1306.0121 [hep-ph]`.

[42] W. Li, “Collective flow from AA, pA to pp collisions – Toward a unified paradigm”, *Nucl. Phys.*, vol. A967, pp. 59–66, 2017. DOI: `10.1016/j.nuclphysa.2017.05.011`. arXiv: `1704.03576 [nucl-ex]`.

[43] E. Gschwendtner *et al.*, “AWAKE, The Advanced Proton Driven Plasma Wakefield Acceleration Experiment at CERN”, *Nucl. Instrum. Meth.*, vol. A829, pp. 76–82, 2016.

[44] T. Acconcia *et al.*, “A Very High Momentum Particle Identification Detector”, *The European Physical Journal Plus*, 2013.

[45] U. W. Heinz and B. V. Jacak, “Two particle correlations in relativistic heavy ion collisions”, *Ann. Rev. Nucl. Part. Sci.*, vol. 49, pp. 529–579, 1999.

[46] A. Kisiel, H. Zbroszczyk, and M. Szymański, “Extracting baryon-antibaryon strong interaction potentials from p$\bar{\Lambda}$ femtoscopic correlation functions”, *Phys. Rev.*, vol. C89, no. 5, p. 054 916, 2014.

[47] TGenPhaseSpace Class Reference, *ROOT Reference Guide*. [Online]. Available: `https://root.cern.ch/doc/v608/classTGenPhaseSpace.html` (visited on 08/03/2018).

[48] E. Braaten and H. .-.-W. Hammer, “Universality in few-body systems with large scattering length”, *Phys. Rept.*, vol. 428, pp. 259–390, 2006.

[49] A. R. Bodmer and Q. N. Usmani, “COULOMB EFFECTS AND CHARGE SYMMETRY BREAKING FOR THE A = 4 HYPERNUCLEI”, *Phys. Rev.*, vol. C31, pp. 1400–1411, 1985. DOI: `10.1103/PhysRevC.31.1400`.